ISSN 0915-633X

NATIONAL INSTITUTE FOR FUSION SCIENCE

Particle Simulation Study of Driven Magnetic Reconnection in a Collisionless Plasma

R. Horiuchi and T. Sato

(Received - May 20, 1994)

NIFS-284

June 1994

RESEARCH REPORT
NIFS Series

NAGOYA, JAPAN

PARTICLE SIMULATION STUDY OF DRIVEN MAGNETIC RECONNECTION IN A COLLISIONLESS PLASMA

Ritoku Horiuchi and Tetsuya Sato

Theory and Computer Simulation Center,

National Institute for Fusion Science,

Nagoya 464-01, Japan

Abstract

Driven magnetic reconnection in a collisionless plasma, "collisionless driven reconnection", is investigated by means of a $2\frac{1}{2}$ dimensional particle simulation. Magnetic reconnection develops in two steps, i.e., slow reconnection which takes place in the early stage of the compression when the current layer is compressed as thin as the orbit amplitude of an ion meandering motion (ion current layer), and subsequent fast reconnection which takes place in the late stage when the electron current is concentrated into the narrow region with spatial scale comparable to the orbit amplitude of an electron meandering motion (electron current layer). The global dynamic evolution of magnetic reconnection is controlled by the physics of the ion current layer. The maximum reconnection rate is roughly in proportion to the driving electric field. It is also found that both ion heating and electron heating take place in accordance with the formation of two current layers and the ion temperature becomes two or more times as high as the electron temperature.

Keywords; particle simulation, driven magnetic reconnection, finite Larmor radius effect, collisionless plasma, two-step evolution

I. Introduction

Magnetohydrodynamic (MHD) studies[1),2)] have disclosed that driven magnetic reconnection plays an essential role on the energy relaxation and the self-organization of a magnetically confined plasma. Under the influence of a driving source and a small amount of electrical resistivity, magnetic reconnection takes place in a time scale much shorter than the resistive time scale and the reconnection rate is primarily determined by the driving electric field.[3)] This process can lead to fast energy conversion from the field energy to the particle energy as well as a topological change of magnetic field.[1)–3)] On the other hand, energetically active phenomena[4)] triggered by magnetic reconnection are often observed in a high temperature, rarefied plasma in which binary collisions between particles are negligible, namely, in a collisionless plasma. It is not so easy to explain how an electric field along the equilibrium current is generated in the neutral sheet of collisionless plasma. The concept of an anomalous resistivity[5)] which originates from the wave-particle interaction or the stochasticity of particle orbit[6)] has been introduced to explain collisionless reconnection. It is widely considered that tearing instability[7)–17)] is one of an effective mechanism for collisionless magnetic reconnection. Particle simulation[13)–17)] has been applied to investigate the collisionless process of magnetic reconnection under a variety of magnetic configuration. Leboeuf et al.[14)] discussed the collisionless magnetic reconnection by means of two-dimensional particle simulation when a small amount of resistivity due to particle collisions was introduced in a periodic simulation domain. They pointed out an importance of the finite Larmor radius effect in current penetration. Hewett et al.[15)] also examined collisionless magnetic reconnection by using an implicit particle simulation code for the case where there existed no external driving force and the initial equilibrium had a current layer the width of which was as thin as the electron skin depth. They found that the time evolution was strongly dependent on the ratio of ion to electron mass.

When a system is subjected to an external driving source or it is macroscopically

unstable, it evolves dynamically with time[3] and thus, the physical parameters, which characterize the state of a system, become a function of time. In this paper we report the simulation of collisionless magnetic reconnection for the case where a plasma is initially in an MHD equilibrium and a driving plasma flow is supplied into a system through the boundary of a simulation domain. Then, the current layer is compressed by the convergent plasma flow and its spatial scale length changes with time. After some period the system dynamically evolves into a kinetic regime in which the finite Larmor radius effect becomes active. In considering such a dynamical evolution it is important to solve self-consistently the nonlinear phenomena including an electron dynamics, an ion dynamics, and the dynamical evolution of the electromagnetic field. For this purpose we have developed an electromagnetic particle simulation code[18)–20)] which can describe not only a finite ion Larmor radius effect but also a finite electron Larmor radius effect in an open system. The purpose of this paper is then to demonstrate the dynamical evolution of driven magnetic reconnection in a collisionless plasma and to clarify the fine mechanism leading to collisionless driven magnetic reconnection. The initial condition and the simulation model are described in Sec. II. We show that two different types of magnetic reconnection take place as a system evolves dynamically. In order to investigate the physical mechanism the dependence of the simulation results on the ion mass, the electron mass and the driving electric field is examined by carrying out several simulation runs. The detailed simulation results are discussed in Sec. III. The detailed analysis of the simulation results reveals that the temporal evolution of magnetic reconnection scales as $E_0^{-1/2} M_i^{1/4}$ and the maximum reconnection rate is roughly in proportion to E_0, where E_0 is the driving electric field at the boundary and M_i is the ion mass. Finally we give a summary of this paper and a physical meaning of the scaling law in collisionless driven magnetic reconnection in connection with the dynamics of current layer in Sec. IV. Comparisons of the simulation results with theoretical studies of the tearing instability are also given in Sec. IV.

II. Simulation model

Let us study externally driven magnetic reconnection of a collisionless plasma by means of two-and-one-half dimensional particle simulation. The semi-implicit method[18)–20)] is used for time advancing. Because both electrons and ions are treated as particles in this method, a finite electron Larmor radius effect can be described as well as a finite ion Larmor radius effect. The physical quantities are assumed to be translationally symmetric in the z-direction ($\frac{\partial}{\partial z} = 0$). The basic equations to be solved are the equations of motion

$$\frac{d(\gamma_j \mathbf{v}_j)}{dt} = \frac{q_j}{m_j}\left[\mathbf{E} + \frac{\mathbf{v}_j}{c} \times \mathbf{B}\right], \tag{1}$$

$$\frac{d\mathbf{x}_j}{dt} = \mathbf{v}_j, \tag{2}$$

and the Maxwell equations

$$\frac{1}{c}\frac{\partial \mathbf{B}}{\partial t} = -\nabla \times \mathbf{E}, \tag{3}$$

$$\frac{1}{c}\frac{\partial \mathbf{E}}{\partial t} = \nabla \times \mathbf{B} - 4\pi \mathbf{j}, \tag{4}$$

$$\nabla \cdot \mathbf{B} = 0, \tag{5}$$

$$\nabla \cdot \mathbf{E} = 4\pi\rho, \tag{6}$$

where $\mathbf{x}_j(t), \mathbf{v}_j(t)$, m_j and q_j are the position, the velocity, the rest mass and the charge of the j-th particle, and the relativistic γ-factor of the j-th particle is defined by

$$\gamma_j = 1/\sqrt{1 - (\mathbf{v}_j \cdot \mathbf{v}_j)/c^2}. \tag{7}$$

The current density $\mathbf{j}(\mathbf{x}, \mathbf{t})$ and the charge density $\rho(\mathbf{x}, t)$ are obtained by summing over all the particles, namely,

$$\mathbf{j}(\mathbf{x}, \mathbf{t}) = \sum_{j=1}^{N} \frac{q_j \mathbf{v}_j(t)}{c} S(\mathbf{x} - \mathbf{x}_j(t)), \tag{8}$$

$$\rho(\mathbf{x}, t) = \sum_{j=1}^{N} q_j \, S(\mathbf{x} - \mathbf{x}_j(t)), \tag{9}$$

where N is the total number of particles and $S(\mathbf{x})$ is the form function of particles which is expressed by a triangle with the base length equal to 2.0 of the grid separation.

As an initial condition we adopt one dimensional equilibrium with the Harris-type anti-parallel magnetic configuration as

$$B_x(y) = B_0 \tanh(y/L), \tag{10}$$

$$P(y) = B_0^2/8\pi \, \mathrm{sech}^2(y/L), \tag{11}$$

where L is the scale height along the y-axis. There is a magnetically neutral sheet along the mid-horizontal line ($y = 0$) in the initial equilibrium. Let us assume that the initial particle distribution is given by the shifted Maxwellian with a spatially constant temperature and the average particle velocity is equal to the diamagnetic drift velocity. Then, the particle position and the particle velocity are determined from the pressure profile $P(y)$ and the current density $\mathbf{j}(\mathbf{x}, 0)$ ($= (0, 0, -B_0/(4\pi L) \, \mathrm{sech}^2(y/L))$). Because both an ion and an electron are loaded to the same spatial position, there is no electric field in the initial profile.

In order to drive magnetic reconnection at the center of simulation domain we adopt the input boundary condition[19] at the boundary of the y-axis ($y = \pm y_b$) and the periodic boundary condition at the boundary of the x-axis ($x = \pm x_b$). At the input boundary the y-derivatives of the field quantities are equal to zero and the plasma is smoothly supplied with the $\mathbf{E} \times \mathbf{B}$ drift velocity into the simulation domain. The driving electric field $\mathbf{E}_d(x,t) = (0, 0, E_{dz}(x,t))$ at the input boundaries is taken to be zero at $t = 0$ and gradually increases for $0 < t < t_A$. After this period ($t > t_A$) $E_{dz}(x,t)$ is described by a constant profile as

$$E_{dz}(x,t) = E_0\{\epsilon_f + (1 - \epsilon_f)(\cos(\phi(x)) + 1)/2\} \tag{12}$$

where

$$\phi(x) = \begin{cases} -\pi & \text{if } x < -x_{b1} \\ \pi x/x_{b1} & \text{if } x_{b1} > x > -x_{b1} \\ \pi & \text{if } x > x_{b1} \end{cases}$$

$\epsilon_f = 0.3$, $x_{b1} = 0.11x_b$, $t_A = 2y_b/v_{A0}$, and v_{A0} is the initial average Alfven velocity. As a boundary condition of the x-axis we have examined two kinds of boundary condition, i.e., 1) free boundary condition[19] under which the x-derivatives of the field quantities are equal to zero and a particle can pass freely through the boundary, and 2) the periodic boundary condition. It is found a posteriori that we have almost the same results for both cases if the simulation box is long enough along the x-axis, say, $x_b/y_b \geq 2.5$. In this paper, therefore, the ratio of the side lengths of the simulation box x_b/y_b is fixed to 3 and the periodic condition is adopted at the boundary of the x-axis.

It is important to examine the numerical accuracy of the simulation model before stepping in the analysis of simulation results. Let us show one example of the numerical tests to find appropriate simulation parameters. Figure 1 shows the temporal evolution of the total magnetic energy for the cases where the total numbers of particles are equal to 120,000, 180,000, 240,000, and 360,000, respectively. Since these simulation results are found to little depend on the particle number, it is appropriate to fix the total number of particles to 240,000 in order to obtain the simulation result independent of the particle number. The simulation domain is implemented on a (66×129) point grid. The time step width Δt is determined so as to satisfy the Courant-Friedrichs-Lewy condition[21] for the electromagnetic wave in vacuum, i.e., the relation $\Delta t = 0.5\Delta y/c$ holds in our simulation where Δy is the grid separation along the y-axis.

III. Simulation results

We carry out several simulation runs with different physical parameters. The relation $L > \rho_i > c/\omega_{pe} > \Delta y$ holds for all cases where ρ_i is the ion Larmor radius, ω_{pe} the electron plasma frequency. Let us first discuss the overview of collisionless driven reconnection by using the simulation result for case A where the ratio of ion to electron mass M_i/M_e is 50, the half-width d_{h0} of the initial mass density profile is $21.9\Delta y$, the initial ion Larmor radius ρ_{i0} is $10.4\Delta y$, the driving electric field E_0 is $-0.04B_0$, $\omega_{pe}/\omega_{ce} = 5.0$, $c/(\omega_{pe}\Delta y) = 2.0$, $\omega_{ce}\Delta t = 0.05$, and ω_{ce} ($= eB_0/M_e c$) is the electron cyclotron frequency. In this case the maximum value of the input flow velocity reaches 0.4 of the local Alfven velocity. Figure 2 shows four snapshots of magnetic flux contours (left) and vector plots of the average ion velocity (right) in the (x, y) plane at $t = 0$, $t = 1.22t_A$, $t = 1.78t_A$, and $t = 2.12t_A$ where the magnetic flux contours less than the initial value at the input boundary are plotted by the dotted line. A magnetically neutral sheet exists along the mid-horizontal line ($y = 0$) and no bulk ion flow exists in the (x, y) plane at $t = 0$ (top panel). An x-shaped structure of magnetic separatrix becomes distinct as a result of magnetic reconnection after the period of $t = 1.22t_A$. The region occupied by the reconnected flux spreads over the whole simulation domain at this time. A fast directed flow arises from the x-point after magnetic reconnection sets in and it carries the reconnected flux toward the boundaries of the x-axis ($x = \pm x_b$). The reconnection point does not always stay at the mid-point of the simulation domain but it shifts slightly along the magnetically neutral sheet with time. One can find in the bottom panel that the shock structure appears in the ion flow pattern.

A. Two-step evolution of collisionless reconnection

Generation of electric field along the equilibrium current is needed for driving magnetic reconnection. Figures 3(a) and 3(b) show (a) the temporal evolution of the z-component

of electric field, which is the reconnection electric filed, and (b) that of the mass density ρ_m (solid line) and the z-component of the current density $-j_z$ (dot-dashed line) at the x-point for case A where the spatial profile of the electric field $E_z(x,0)$ along the neutral sheet is expanded into the fourier series and the amplitude $E_z^{(1)}$ of the $n = 1$ mode is plotted in the logarithmic scale in the left panel, while the mass density and the current density are plotted in the linear scale in the right panel. There are three temporal phases in the evolution of the reconnection electric field $E_z^{(1)}$, i.e., the initial phase ($0 < t < 0.6t_A$), the slow reconnection phase ($0.6t_A < t < 1.3t_A$), and the fast reconnection phase ($1.3t_A < t < 1.8t_A$). The reconnection electric field $E_z^{(1)}$ remains at the noise level in the initial phase. The electric field begins to grow slowly when both the mass density and the current density start increasing in the current layer as a result of the compression by the convergent plasma flow in the slow reconnection phase. The growth rate γ_g of the electric field is estimated to be $0.92/t_A$ or $0.103\omega_{ci}$ where ω_{ci} ($= eB_0/M_ic$) is the ion cyclotron frequency. The inclination of the growth curve becomes steeper suddenly after the mass density reaches the maximum value at $t \approx 1.3t_A$. The mass density tends to decrease slowly in the fast reconnection phase while the current density continues to increase. The growth rate of the electric field in the fast reconnection phase is estimated to be $6.0/t_A$ or $0.013\omega_{ce}$. This value is much larger than the growth rate in the slow reconnection phase. These results suggest that magnetic reconnection in the fast reconnection phase is controlled by the mechanism different from that in the slow reconnection phase.

Let us examine the behaviors of the physical quantities in the slow reconnection phase. Figures 4(a), 4(b), and 4(c) show (a) the spatial profiles of the electron temperature T_e (solid line) and the ion temperature T_i (dotted line), and (b) those of the z-component of the average electron velocity (solid line) and the z-component of the average ion velocity (dotted line), and (c) those of the mass density (solid line) and the z-component of the current density (dotted line) at $t = 1.0t_A$ where the profiles are plotted along the

vertical line passing on the reconnection point ($(x, y) = (-2.5\Delta x, 0)$) and the particle temperature is obtained by assuming that the distribution function is approximated by the shifted Maxwellian. The equilibrium current is initially dominated by the diamagnetic component. In other words, the electron current is equal to the ion current because $T_e = T_i$ at $t = 0$. The electron current becomes dominant over the ion current because of its small inertia as time goes on. It is worthy to note that the mass density profile has the same width as the current density profile. In the vicinity of the magnetically neutral sheet an ion executes a meandering motion[20] due to finite ion Larmor radius effect. This motion creates the negative ion current at the edge region of the current layer. The ion motion is rather free from magnetic field in the inner region of the current layer while it is strongly restricted by the motion of magnetic field outside the current layer. When the current layer is compressed by increasing magnetic pressure, ions inside the current layer feel as if they are compressed by two walls approaching each other. The interaction between ions and the moving magnetic walls results in the ion heating through the Fermi mechanism, as was seen in Fig. 4(a). On the contrary, an electron moves together with the magnetic field without interacting with the magnetic wall because the electron Larmor radius ρ_e is much smaller than the width of the current layer. Thus, the electron temperature remains almost constant in the slow reconnection phase.

Let us examine what happens in the transition period between the slow reconnection phase and the fast reconnection phase. Figures 5(a) and 5(b) show (a) the temporal evolutions of the half-width d_h of the mass density profile (solid line), the half-width d_{jz} of the current density profile (dotted line) along the y-axis, the average orbit amplitude l_{mi} of meandering ions (dashed line) and the average orbit amplitude l_{me} of meandering electrons (dot-dashed line), and (b) those of the electron number density (dotted line) and the ion number density (solid line) at the x-point where $l_{mi} = \sqrt{d_h \rho_i}$, $l_{me} = \sqrt{d_h \rho_e}$, the spatial scales d_h, d_{jz}, l_{mi}, and l_{me} in Fig. 5(a) are normalized by Δy, and $d_{jz} \approx d_h$ (

$= 0.863L$) at $t = 0$. Both the mass density profile and the current density profile have initially half-width of about 2 ρ_{i0} where the initial ion Larmor radius ρ_{i0} is equal to $10.4\Delta y$. Both d_h and d_{jz} decrease with the same rate in the compression time scale in the first half of the slow reconnection phase. The change of d_h slows down and it approaches l_{mi} in the latter half of the slow reconnection phase. The half-width d_{jz} continues to decrease during the slow reconnection phase and it approaches l_{me} at the end of the slow reconnection phase. Both d_h and d_{jz} remain almost constant in the fast reconnection phase where $d_{jz} \approx 3\Delta y$ and $d_h \approx 8\Delta y$. Thus, the electric current is localized in a narrower region than the mass density in the fast reconnection phase.

The number density at the x-point begins to increase at $t \approx 0.6t_A$, as is seen in Fig. 5(b). Both the electron density and the ion density increase with the same growth rate during the slow reconnection phase. The growth of the number density slows down and the density becomes maximum at the end of the slow reconnection phase. In the fast reconnection phase the electron density becomes dominant over the ion density. Comparing Fig. 5(a) with Fig. 5(b), one can find that the charge separation becomes distinct after the scale height of the mass density profile becomes nearly equal to the ion Larmor radius, i.e., $d_h \approx l_{mi} = \sqrt{d_h \rho_i}$. This phenomenon can be easily understood by the finite ion Larmor radius effect in the vicinity of the neutral sheet.[14] That is, most of the ions in the current layer become unmagnetized when $d_h \approx \rho_i$, while the electrons remain magnetized. Therefore, the input flow (Poynting flux) no longer works on thinning the ion current layer but acts to increase the ion temperature in it. For the electrons, however, compression can still keep working. Consequently, the charge neutrality condition is violated in the central region of the current layer, when the fast reconnection phase sets in.

Let us examine the behaviors of the physical quantities in the fast reconnection phase in detail. Figures 6(a), 6(b), and 6(c) show (a) the ion temperature profiles, (b) the electron temperature profiles, and (c) the spatial profiles of the z-component of the current

density at three different periods where the solid, dotted, and dashed lines correspond to the spatial profiles along the vertical line (y-axis) passing on the reconnection point at $t = 1.0t_A$, $t = 1.39t_A$, and $t = 1.78t_A$, respectively. The ion temperature takes a broad profile with a spatial scale comparable to l_{mi} and its peak value increases monotonously during both the slow reconnection phase and the fast reconnection phase. On the contrary, the electron temperature keeps a fairly flat profile during the slow reconnection phase, but increases suddenly in the narrow region comparable to the orbit amplitude l_{me} of an electron meandering motion as soon as the fast reconnection phase starts. The ion temperature is about two times as high as the electron temperature in the central region of the current layer in the fast reconnection phase.

It is interesting to notice in Fig. 6(c) that there are two spatial scales in the current density profile, i.e., the orbit amplitude l_{mi} of an ion meandering motion and the orbit amplitude l_{me} of an electron meandering motion. The current density profile with the large spatial scale of l_{mi}, " ion current layer ", develops in the slow reconnection phase and is maintained in the fast reconnection phase. The peaked profile with the small spatial scale of l_{me}, " electron current layer ", emerges inside the large scale profile and grows rapidly in the fast reconnection phase. The separation of the current density into two, broad and narrow, spatial profiles is due to the dominance of either the finite ion Larmor radius effect or the finite electron Larmor radius effect. The ion current is dominant in the outer region of the current layer while the electron current is dominant in the inner region in the fast reconnection phase.

Comparing Fig. 6(b) with Fig. 6(c), one can find that the abrupt electron heating takes place in the electron current layer in the final phase of fast reconnection, i.e., $t = 1.78t_A$. This phenomenon indicates that as the current layer is compressed as thin as l_{me}, the driving flow acts no longer to thin the current layer but acts to increase the temperature of meandering electrons in it, similarly as we have observed for the ions

when the current layer becomes as thin as the ion Larmor radius.

Figure 7 shows the contour maps of the mass density (top), the z-component of the current density (second), the electron temperature (third), and the ion temperature (bottom) in the (x, y) plane at $t = 1.78t_A$ where a contour with a smaller value than the average one is plotted by the dotted line. Most of the plasma, which exists inside the current layer in the slow reconnection phase, is carried away by the divergent plasma flow toward the boundaries of the x-axis (Fig. 2), and thus the mass density tends to take a fairly flat profile in the current layer in the fast reconnection phase. The electric current is enhanced in the long and narrow region between two peakings of the mass density. The half-width of the current layer is comparable to the orbit amplitude of an electron meandering motion, as was seen in Figs. 5(a) and 6(c). The electron temperature profile is very similar to the the current profile since the electron heating takes place exclusively in the electron meandering layer, which is equivalent to the peaked current layer. On the contrary, the ion temperature takes a broad profile with the half-width nearly equal to l_{mi}, which is caused by the compressional heating of meandering ions by the convergent plasma flow.

B. Dependence on ion mass

It is important to examine the parameter dependence of the simulation results in considering the physical mechanism of collisionless driven reconnection. We carry out several simulation runs with a various set of physical parameters. The simulation parameters are listed in Table 1. The dependence on the ion mass is examined by using the simulation results for case A, case B, and case C where the simulation parameters are chosen so that the parameters associated with the ion mass, say, the ion Larmor radius, the Alfven velocity, and so on, are different while keeping the others fixed. One aspect of the results is shown in Figure 8 where the temporal evolutions of the z-component of the electric

field $E_z^{(1)}$ at the reconnection point for case A (dotted line), case B (solid line), and case C (dashed line) are plotted in the logarithmic scale. Note in Fig.8 that the time is normalized by using the electron cyclotron frequency ω_{ce} which is independent of the ion mass. The growth of the electric field becomes slower as the ion mass or ion Larmor radius increases. This result corresponds to the fact that the compression speed of the current layer decreases as the ion mass increases. On the other hand, the saturated reconnection rate or the peak value of the electric field is almost independent of the ion mass. By changing the normalization of time it is found that three evolution curves agree fairly well with one another if the quantity in proportion to $M_i^{1/4}$ is introduced as a normalization of time, as is shown in Fig. 9. That is, the whole temporal evolution of collisionless driven reconnection is characterized by the time scale in proportion to $M_i^{1/4}$, namely, irrespective of whether the evolution stage is the slow reconnection stage or fast. Figures 10(a) and 10(b) show (a) the temporal evolutions of the ion temperature and (b) those of the electron temperature at the reconnection point for the same cases as Fig. 8 where a closed circle, an open circle, and an open square correspond to the simulation results for case A, case B, and case C, respectively. The ion temperature increases in proportion to $M_i^{1/2}$ in the fast reconnection phase, while the electron heating takes place independent of the ion mass. These results suggest that the dynamical evolution of collisionless driven reconnection and the ion heating are controlled by a physical mechanism associated with the ion dynamics, but that the electron heating is caused by the mechanism independent of the ion mass. We will give a phenomenological explanation of these results in connection with the dynamics of the ion current layer in the next section.

C. Dependence on electron mass

The dependence on the electron mass is examined by using the simulation results for case A, case D, and case E where the ion mass is fixed. Figure 11 shows the temporal

evolutions of the z-component of the electric field $E_z^{(1)}$ at the reconnection point for case A (dotted line), case D (solid line), and case E (dashed line) where the time is normalized by the Alfven transit time. In contrast to the cases shown in Fig. 8, there is not any significant difference among three cases except the fact that the noise level in the initial phase depends weakly on the electron mass. In other words, the development of the reconnection field depends little on the electron mass, although most of the electric current in the vicinity of the reconnection point is carried by electrons and the width of the current layer is given by the small spatial scale associated with the electron mass in the fast reconnection phase. Figures 12(a) and 12(b) show (a) the temporal evolutions of the ion temperature and (b) those of the electron temperature at the reconnection point for the same cases as Fig. 11 where an open circle, a closed circle, and an open square correspond to the results for case D, case A, and case E, respectively. The electron temperature increases slowly as soon as the slow reconnection phase starts and a small but apparent difference appears among three cases. It remains nearly constant for a while, and then increases rapidly in the fast reconnection phase. The electron heating takes place more efficiently as the electron mass becomes larger. It is found that the electron temperature scales as $M_e^{1/4}$ in the fast reconnection phase. In contrast to the electron temperature the ion temperature increases independent of M_e. These results indicate that while the ion heating is caused by the compressional heating of meandering ions, the electron heating is a process of pure electron dynamics. The proportionality of the electron temperature to an electron mass, $M_e^{1/4}$, suggests that the electron heating must result from energization of meandering electrons in the narrow current layer subject to the incoming Poynting flux from the external region.

D. Dependence on driving electric field

According to the MHD studies[3] the reconnection rate depends strongly on the driving electric field E_0. Let us examine the dependence of the reconnection rate in a collisionless plasma on the driving electric field. Figure 13 shows the temporal evolutions of the z-component of the electric field $E_z^{(1)}$ at the reconnection point for case A (dotted line), case F (solid line), and case G (dashed line) where the time is normalized by the Alfven transit time t_A. Magnetic reconnection starts earlier and the electric field grows faster as the driving electric field becomes larger. The detailed examination reveals that the evolution time of magnetic reconnection scales as $E_0^{-1/2}$. This reflects the fact that the compression speed of the current layer depends strongly on the input rate of the magnetic flux through the boundary, i.e., the driving electric field E_0. The saturated reconnection rate or the peak value of electric field is roughly in proportion to E_0. This result is in good agreement with that of the MHD studies[3] where the reconnection rate is approximately given by the external driving electric field and depends little on the value of the electric resistivity.

Figures 14(a) and 14(b) show (a) the temporal evolutions of the ion temperature and (b) those of the electron temperature at the reconnection point for the same cases as Fig. 13 where the temperature is plotted in the same normalization unit. Both the electron heating and the ion heating take place more efficiently as the driving electric field becomes larger. The ion temperature is always higher than the electron temperature irrespective of the driving electric field except the initial phase. The ion temperature is two or more times as high as the electron temperature in the fast reconnection phase. These results indicate that the plasma compression becomes stronger as the driving electric field increases, and thus, reconnection and collisionless plasma heating take place more efficiently. We will slightly touch on a physical meaning of the scaling law with E_0 in the next section.

IV. Summary and Discussions

We have investigated driven magnetic reconnection in a collisionless plasma by means of a $2\frac{1}{2}$ dimensional particle simulation for the case where the current layer is compressed by the convergent plasma flow which is supplied through the boundary by the external electric field. The main results are summarized as follows.

(1) Driven magnetic reconnection consists of three temporal phases, i.e., the initial phase in which the electric field remains at the noise level ($t < 0.6t_A$), the slow reconnection phase ($0.6t_A < t < 1.3t_A$), and the fast reconnection phase ($1.3t_A < t < 1.8t_A$).

(2) The reconnection electric field grows at the reconnection point with a slow growth rate of the order of roughly $0.1\omega_{ci}$ while both the current layer and the mass density are equally being compressed.

(3) When the width of the current layer is compressed as thin as the orbit amplitude of an ion meandering motion, the ions in the current layer become unmagnetized while the electrons remain magnetized. Only magnetized drifting electrons can carry the Poynting (magnetic) flux inside the current layer, thereby enhancing the electron current in a narrow layer with the spatial scale of the orbit amplitude of meandering electrons. Thus, the current layer is split into the ion one and the electron one in the fast reconnection phase. Magnetic reconnection takes place with a fast growth rate of $0.01\omega_{ce}$ in good accordance with this enhanced narrow electron current layer.

(4) The evolution time of magnetic reconnection scales as $E_0^{-1/2}M_i^{1/4}$, but it depends little on the electron mass. That is, magnetic reconnection develops faster as the ion mass decreases and/or the driving electric field increases. The maximum reconnection rate is roughly in proportion to the driving electric field but independent of both the ion mass and the electron mass.

(5) Only the ion heating takes place inside the current layer in the slow reconnection

phase. In the fast reconnection phase the ion heating takes place inside the broad ion current layer, while the electron heating takes place only inside the narrow electron current layer. The ion temperature is two or more times as high as the electron temperature during the reconnection process.

Let us here give a phenomenological explanation of the scaling law of $E_0^{-1/2}M_i^{1/4}$ by using a simple model of the current layer. Suppose that both an ion and an electron are magnetized outside the ion current layer, while an ion is unmagnetized and an electron is magnetized inside the ion current layer. A convergent plasma flow carries the magnetic field from the boundary of the simulation box towards the ion current layer and compresses it. Since magnetized drifting electrons can penetrate through the ion current layer, magnetic flux can be carried inside.[14),22)] Thus, the ion current layer dynamically evolves with satisfying the balance between the plasma compression by the convergent plasma flow and the penetration of the magnetic flux into the ion current layer.

Figures 15(a) and 15(b) show (a) the temporal evolutions of the magnetic field B_b at the current boundary for case A (closed circle), case B (open circle) and case C (open square), and (b) those for case A (open square), case F (open circle) and case G (closed circle) where the time is normalized by $(M_i/M_e)^{1/4}/\omega_{ce}$ in Fig. 15(a), and by $(E_0/B_0)^{-1/2}t_A$ in Fig. 15(b). It is found in Fig. 15(a) and Fig. 15(b) that the maximum value of magnetic field B_b at the current boundary, which is listed in Table 2, changes according to the scaling law of $B_b \propto E_0^{1/2}M_i^{1/4}$. Though not shown here, the electric field E_b at the current boundary is observed to be proportional to the driving electric filed E_0. Since the penetration speed v_{pn} of magnetic field into the current layer is represented by the $\mathbf{E} \times \mathbf{B}$ drift velocity,[14)] we have the relation as $v_{pn} \propto E_0^{1/2}M_i^{-1/4}$. This scaling law is in good agreement with the inverse of the scaling law of the dynamical evolution time of magnetic reconnection. We conclude that the penetration speed at the ion current boundary determines the whole dynamical evolution of collisionless driven reconnection.

It has been clarified by our simulation study that there exist two types of physical mechanism leading to magnetic reconnection in a collisionless plasma. One is responsible for the slow reconnection process associated with the ion meandering motion and the other is responsible for the fast reconnection process associated with the electron meandering motion. When the width of the current layer becomes comparable to the orbit amplitude of the ion meandering motion, the rate of magnetic reconnection due to the ion meandering motion is dominant over that due to the electron meandering motion. The penetration of magnetic field into the current layer splits the current layer into the ion one and the electron one by compressing only electrons within the ion current layer. The Poynting flux into the ion current layer results in the increase of the ion temperature and the enhancement of the electric current. Since the ion temperature is always higher than the electron temperature, the magnetic pressure is roughly balanced with the ion thermal pressure. The pressure balance reduces to $T_i \propto E_0^{1/2} M_i^{1/2}$ where we use the observed scaling law of the number density n_{in} at the center of the current layer, i.e., $n_{in} \propto E_0^{1/2}$. This scaling law of the ion temperature is consistent with that of the simulation results shown in Fig. 10(a) and Fig. 14(a). When the electron current layer is compressed as thin as the orbit amplitude of the electron meandering motion, the thinning of the electron current layer is stopped. After this period the rate of magnetic reconnection due to the electron meandering motion is dominant over that due to the ion meandering motion. The electric field E_z at the reconnection point increases with the growth rate of fast reconnection until it reaches the input rate of magnetic field at the boundary of the simulation domain, i.e., the driving electric field E_0. Thus, the maximum reconnection rate is roughly in proportion to the driving electric field.

We have discussed the simulation results without specifying the physical mechanism responsible for driven magnetic reconnection in a collisionless plasma. It is widely believed that a collisionless tearing instability[7)–17)] is an effective mechanism for collisionless mag-

netic reconnection. Let us first consider the triggering mechanism of the collisionless reconnection in the slow phase. The linear growth rate of the ion tearing instability[17] is estimated to be $\gamma_t \approx 0.08\omega_{ci}$ for a thin current layer ($d_{jz} \approx 2\rho_{i0}$). This value is in good agreement with the simulation results of $\gamma_g \approx 0.103\omega_{ci}$ in the slow reconnection phase. This agreement suggests that the slow reconnection can be triggered by the ion tearing instability associated with the ion meandering motion.

One can immediately come up with the electron tearing instability[7),8),10)–12)] for the fast reconnection process. The linear growth rate γ_e of the electron tearing instability[7)] is estimated to be $\gamma_e \approx 0.02\omega_{ce}$ if the relations $d_{jz} \approx l_{me}$ and $\gamma_e \approx (\rho_e/d_{jz})^{5/2}\omega_{ce}$ are used. This value appears not disagreeable with the simulation results of $\gamma_g \approx 0.013\omega_{ce}$ in the fast reconnection phase and the half-width of the electron current layer is in good agreement with the theoretical value of $l_{me} = \sqrt{d_h\rho_e}$ inside which the resonant wave-particle interaction takes place.[11)] Thus, fast reconnection may be able to be attributed to the electron tearing instability. If so, however, we fall into a complete conflict with the obtained scaling law as $E_0^{-1/2}M_i^{1/4}$ which is independent of the electron dynamics. Remember, however, that all the electron parameters such as the electron cyclotron frequency and the electron Larmor radius are not time-independent but strongly time-variable. It is quite likely that the local electron parameters are so adjusted as to match the external macroscopic dynamics and the apparent dynamical behavior appears to be controlled by the ion dynamics, although in fact the evolution is governed by the local electron dynamics which is highly susceptible to the surrounding macroscopic condition.

Before concluding this paper, let us point out two important problems to be studied in the near future. First, an electron flow with a large bulk velocity along the z-axis was observed in the fast reconnection phase in our simulation. This fact suggests a possibility that the electron flow would excite kinetic waves such as the lower-hybrid-drift mode[5)], thereby anomalous resistivity being generated to cause collisionless magnetic reconnection.

Investigation of this effect requires a really three dimensional treatment. Secondly, in the fast reconnection phase the electron current layer is found to become as thin as the orbit amplitude of the electron meandering orbit. However, its width is three times of the grid size along the y-axis, i.e., $d_{jz} \approx 3\Delta y$. Furthermore, the electron skin depth c/ω_{pe} is typically equal to $2\Delta y$. These values are close to the lower limit of the spatial resolution in the numerical calculation, i.e., the grid separation Δy. Thus, we are now carrying out simulation runs with a higher spatial resolution than that in the present study in order to make the simulation results more physically comprehensive and reliable.

Acknowledgments

The authors are grateful to Professors S. Bazdenkov, K. Watanabe and T. Hayashi for their continuous interests in this work. The simulation work was performed by employing the Advanced Computing System for Complexity Simulation at the National Institute for Fusion Science (NIFS).

This work was supported in part by a Grant-in-Aid from the Ministry of Education, Science and Culture in Japan (No. 03044157 and No. 05836038).

References

1. R. Horiuchi and T. Sato, Phys. Rev. Lett. **55**, 211(1985); R. Horiuchi and T. Sato, Phys. Fluids **29**, 1161, 4174(1986), 1142(1988).

2. T. Sato, Y. Nakayama, T. Hayashi, K. Watanabe, and R. Horiuchi, Phys. Rev. Lett. **63**, 528(1989); M. Yamada, Y. Ono, A. Hayakawa, M. Katsurai, and F. W. Perkins, Phys. Rev. Lett. **65**, 721(1990); R. Horiuchi and T. Sato, Phys. Fluids B 4, 672(1992).

3. T. Sato and T. Hayashi, Phys. Fluids **22**, 1189(1979); T. Sato, T. Hayashi, K. Watanabe, R. Horiuchi, M. Tanaka, N. Sawairi and K. Kusano, Phys. Fluids B 4, 450(1992).

4. E. R. Priest, *Solar Magnetohydrodynamics* (Dordrecht,Reidel,1982); A. Nishida, *Geomagnetic Diagnostics of the Magnetoshpere* (Springer-Verlang, New York, 1978).

5. For example, R. C. Davidson and N. T. Gladd, Phys. Fluids **18**, 1327(1975); P. C. Liewer and R. C. Davidson, Nucl. Fusion **17**, 85(1977); A. A. Galeev and R. Z. Sagdeev, *Basic Plasma Physics II* (North-Holland Physics Publishing, New York, 1984), p.271; M. Tanaka and T. Sato, J. Geophys. Res. **86**, 5541(1981).

6. W. Horton and T. Tajima, Geophys. Res. Lett. **17**, 123(1990).

7. G. Laval, R. Pellat, and M. Vuillemin, *Plasma Physics and Controlled Fusion Research* (International Atomic Energy Agency, Vienna, 1966), Vol. II, p. 259.

8. B. Coppi, G. Laval, and R. Pellat, Phys. Rev. Lett. **16**, 1207(1966).

9. K. Schinder, J. Geophys. Res. **79**, 2803(1974).

10. J. D. Drake and Y. C. Lee, Phys. Rev. Lett. **39**, 453(1977).

11. A. A. Galeev, *Basic Plasma Physics II* (North-Holland Physics Publishing, New York, 1984), p.305.

12. X. Wang and A. Bhattacharjee, J. Geophys. Res. **98**, 19419(1993).

13. I. Katanuma and T. Kamimura, Phys. Fluids **23**, 2500(1980).

14. J. N. Leboeuf, T. Tajima and J. M. Dawson, Phys. Fluids **25**, 784(1982).

15. D. W. Hewett, G. E. Frances and C. E. Max, Phys. Rev. Lett. **61**, 893(1988).

16. W. Zwingmann, J.Wallance, K. Schindler, and J. Birn, J. Geophys. Res. **95**, 20877(1990).

17. P. L. Pritchett, F. V. Coroniti, R. Pellat, and H. Karimabadi, J. Geophys. Res. **96**, 11523(1991).

18. M. Tanaka and T. Sato, Phys. Fluids **29**, 3823(1986).

19. S. Murakami and T. Sato, J. Phys. Soc. Japan **61**, 849(1992).

20. R. Horiuchi and T. Sato, Phys. Fluids B **2**, 2652(1990).

21. R. Courant, K. O. Friedrichs, and H. Lewy, Math. Ann. **100**, 32(1928).

22. A. Fruchtman and K. Gomberoff, Phys. Fluids B **5**, 2371(1993).

Figure captions

Fig. 1. Temporal evolution of the total magnetic energy for four test runs where the total numbers of particles are equal to 120,000 (dot-dashed line), 180,000 (dashed line), 240,000 (dotted line), and 360,000 (solid line), respectively.

Fig. 2. Time sequences of magnetic flux contours (left) and vector plots of the average ion velocity (right) in the (x, y) plane at $t = 0$, $t = 1.22t_A$, $t = 1.78t_A$, and $t = 2.12t_A$ for case A where the magnetic flux contours less than the initial value at the input boundary ($y = \pm y_b$) are plotted by the dotted line.

Fig. 3. Temporal evolutions of (a) the reconnection electric field, and (b) the mass density ρ_m (solid line) and the z-component of the current density $-j_z$ (dot-dashed line) at the x-point for case A. Note that the amplitude $E_z^{(1)}$ of the $n = 1$ mode along the neutral sheet is plotted in the logarithmic scale in the left panel while the mass density and the current density are plotted in the linear scale in the right panel. Three fitting functions of $E_z^{(1)}(t) = c_0$ ($0 < t < 0.6t_A$), $E_z^{(1)}(t) \propto \exp(0.92t/t_A)$ ($0.6t_A < t < 1.3t_A$), and $E_z^{(1)}(t) \propto \exp(6.0t/t_A)$ ($1.4t_A < t < 1.7t_A$) are also plotted in Fig. 3(a) for comparison.

Fig. 4. Spatial profiles of (a) the electron temperature T_e (solid line) and the ion temperature T_i (dotted line), (b) the z-component of the average electron velocity (solid line) and the z-component of the average ion velocity (dotted line), and (c) the mass density (solid line) and the z-component of the current density (dotted line) at $t = 1.0t_A$ for case A where the profiles along the vertical line passing on the reconnection point are plotted.

Fig. 5. Temporal evolutions of (a) the half-width d_h of the mass density profile (solid line), the half-width d_{jz} of the current density profile (dotted line) along the y-axis, the average orbit amplitude l_{mi} of meandering ions (dashed line) and the

average orbit amplitude l_{me} of meandering electrons (dot-dashed line), and (b) the electron number density (dotted line) and the ion number density (solid line) at the x-point for case A where the spatial scales d_h, d_{jz}, l_{mi}, and l_{me} are normalized by the grid separation Δy along the y-axis.

Fig. 6. Spatial profiles of (a) the ion temperature, (b) the electron temperature, and (c) the z-component of the current density at $t = 1.0t_A$ (solid line), $t = 1.39t_A$ (dotted line), and $t = 1.78t_A$ (dashed line) for case A where the profiles along the vertical line passing on the reconnection point are plotted. The average orbit amplitude l_{mi} of meandering ions and the average orbit amplitude l_{me} of meandering electrons which are estimated at $t = 1.78t_A$ are also drawn with arrows for comparison.

Fig. 7. Contour maps of the mass density, the z-component of the current density, the electron temperature, and the ion temperature in the (x, y) plane at $t = 1.78t_A$ for case A where a contour with a smaller value than the average one is plotted by the dotted line.

Fig. 8. Temporal evolutions of the reconnection electric field for three different ion masses with a fixed electron mass and a fixed driving electric field, i.e., $\rho_{i0}/\Delta y = 7.4$ (case B), 10.4 (case A), and 15.1 (case C).

Fig. 9. The same figure as Fig. 8, but the abscissa is replaced by $t\omega_{ce}(M_i/M_e)^{-1/4}$. Note that the electron mass is fixed for three cases.

Fig. 10. Temporal evolutions of (a) the ion temperature and (b) the electron temperature at the reconnection point for the same cases as Fig. 8 where an open circle, a closed circle, and an open square correspond to the simulation results for case B, case A, and case C, respectively.

Fig. 11. Temporal evolutions of the reconnection electric field for three different electron masses with a fixed ion mass and a fixed driving electric field, i.e., $\omega_{pe}/\omega_{ce} = 3.5$ (case D), 5.0 (case A), and 7.07 (case E).

Fig. 12. Temporal evolutions of (a) the ion temperature and (b) the electron temperature at the reconnection point for the same cases as Fig. 11 where an open circle, a closed circle, and an open square correspond to the simulation results for case D, case A, and case E, respectively.

Fig. 13. Temporal evolutions of the reconnection electric field for three different driving fields with a fixed ion mass and a fixed electron mass, i.e., $E_0/B_0 = -0.01$ (case F), -0.02 (case G), and -0.04 (case A).

Fig. 14. Temporal evolutions of (a) the ion temperature and (b) the electron temperature at the reconnection point for the same cases as Fig. 13.

Fig. 15. Temporal evolutions of the magnetic field at the current boundary (a) for the same cases as Fig. 8, and (b) for the same cases as Fig. 13. Here the time is normalized by $(M_i/M_e)^{1/4}/\omega_{ce}$ in Fig. 15(a), and by $(E_0/B_0)^{-1/2}t_A$ in Fig. 15(b).

Table 1: Simulation parameters

case	M_i/M_e	$\rho_{i0}/\Delta y$	$d_{h0}/\Delta y$	E_0/B_0	ω_{pe}/ω_{ce}
A	50	10.4	21.9	-0.04	5.0
B	25	7.4	21.9	-0.04	5.0
C	100	15.1	21.9	-0.04	5.0
D	25	10.4	21.9	-0.04	3.5
E	100	10.4	21.9	-0.04	7.07
F	50	10.4	21.9	-0.01	2.0
G	50	10.4	21.9	-0.02	2.0

Table 2: Magnetic field at ion current boundary

case	A	B	C	F	G
M_i/M_e	50	25	100	50	50
E_0/B_0	-0.04	-0.04	-0.04	-0.01	-0.02
B_b/B_0	3.4	2.7	4.1	1.9	2.5

Figure 1

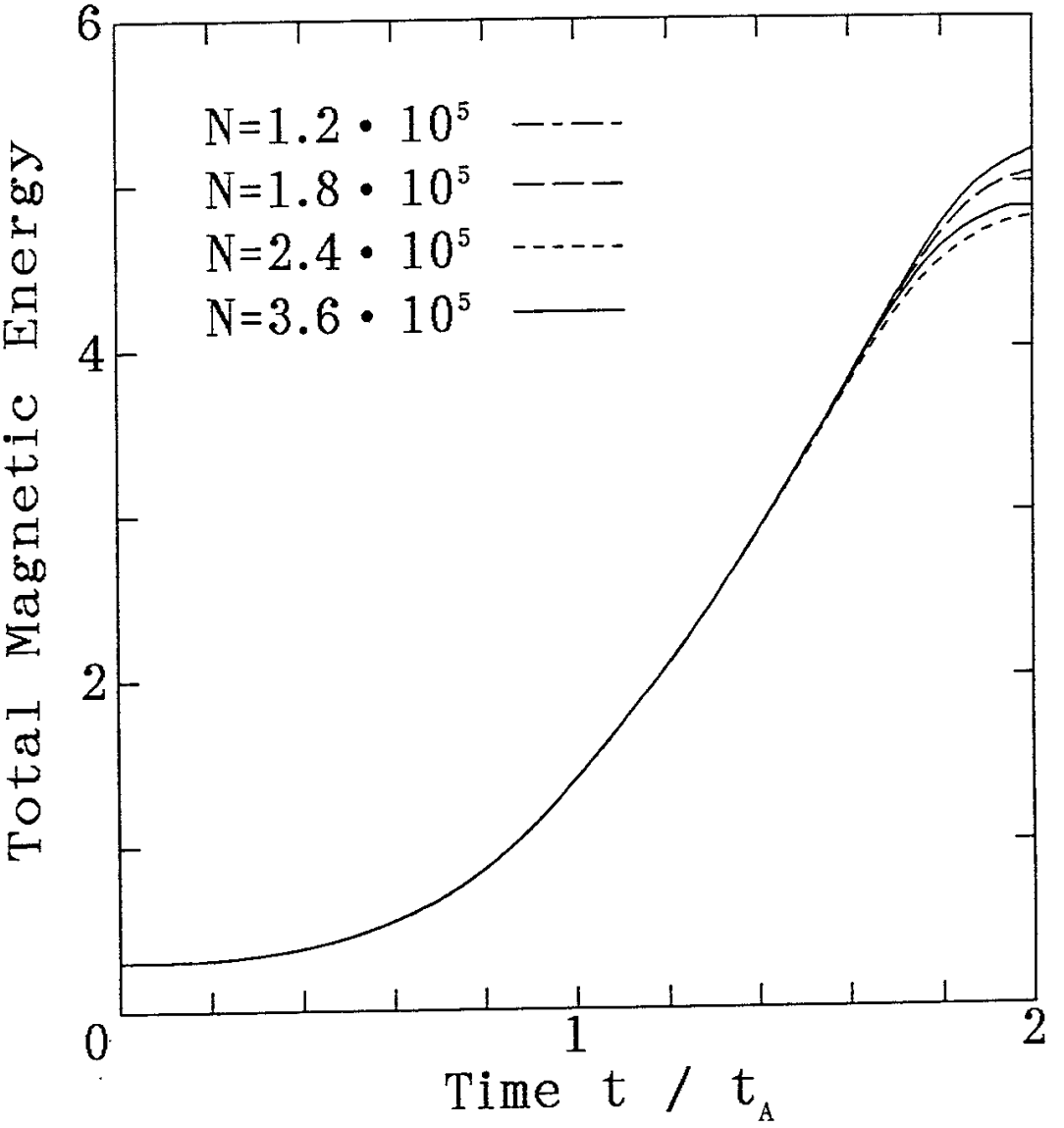
Total Magnetic Energy
6
4
2
0
1
2
Time t / t_A
N=1.2 • 10^5
N=1.8 • 10^5
N=2.4 • 10^5
N=3.6 • 10^5

Figure 2

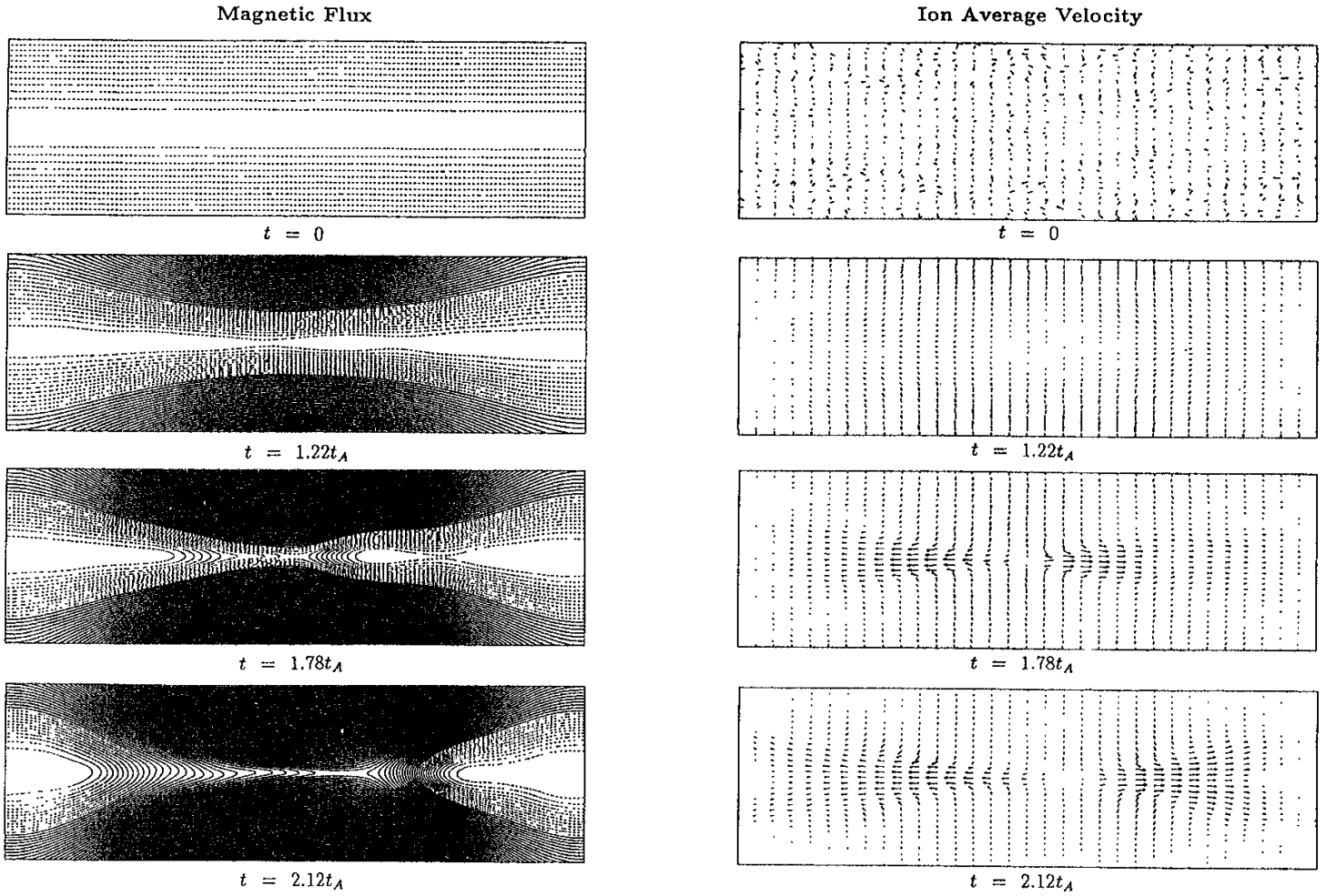
Magnetic Flux
Ion Average Velocity
$t = 0$
$t = 0$
$t = 1.22t_A$
$t = 1.22t_A$
$t = 1.78t_A$
$t = 1.78t_A$
$t = 2.12t_A$
$t = 2.12t_A$

Figure 3

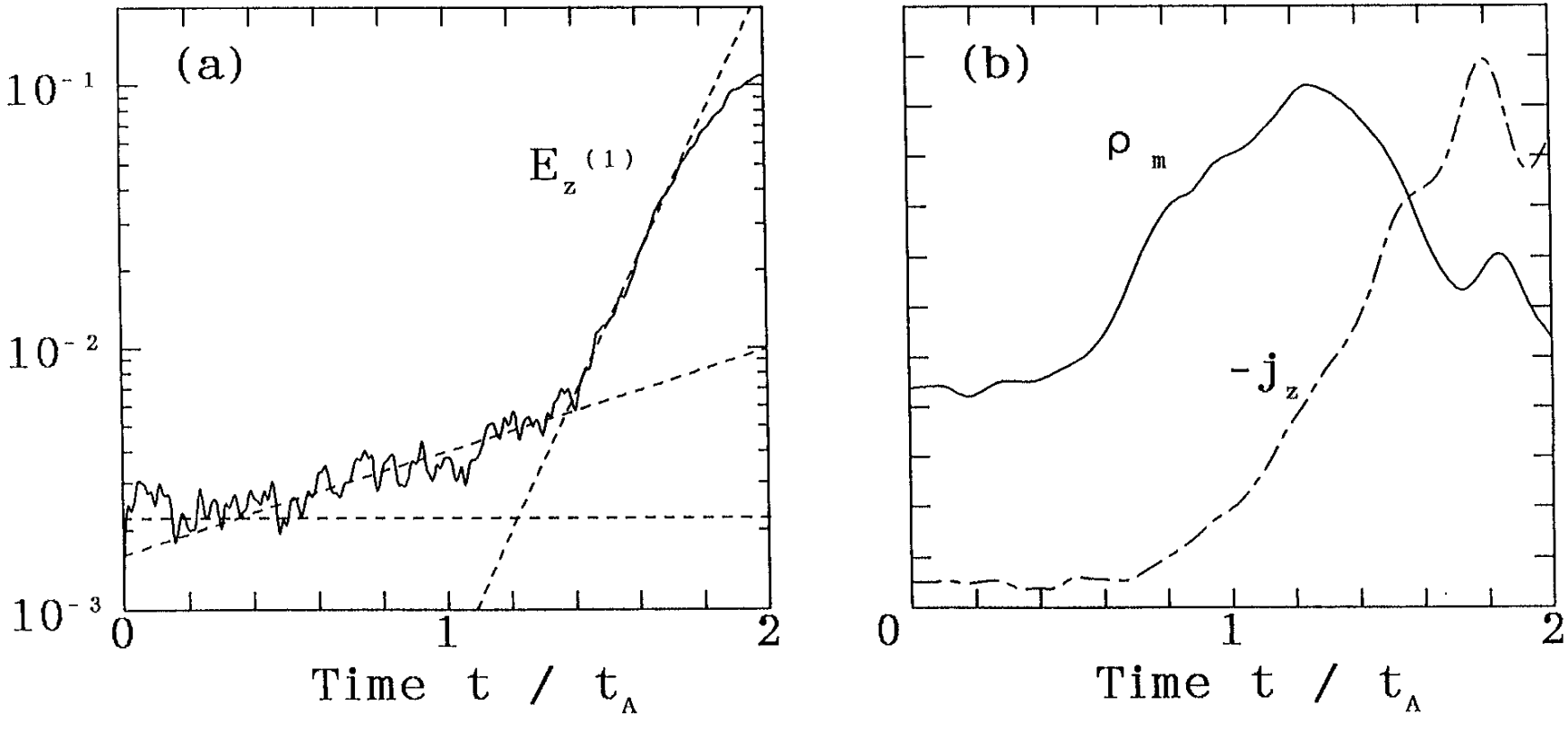

Figure 4

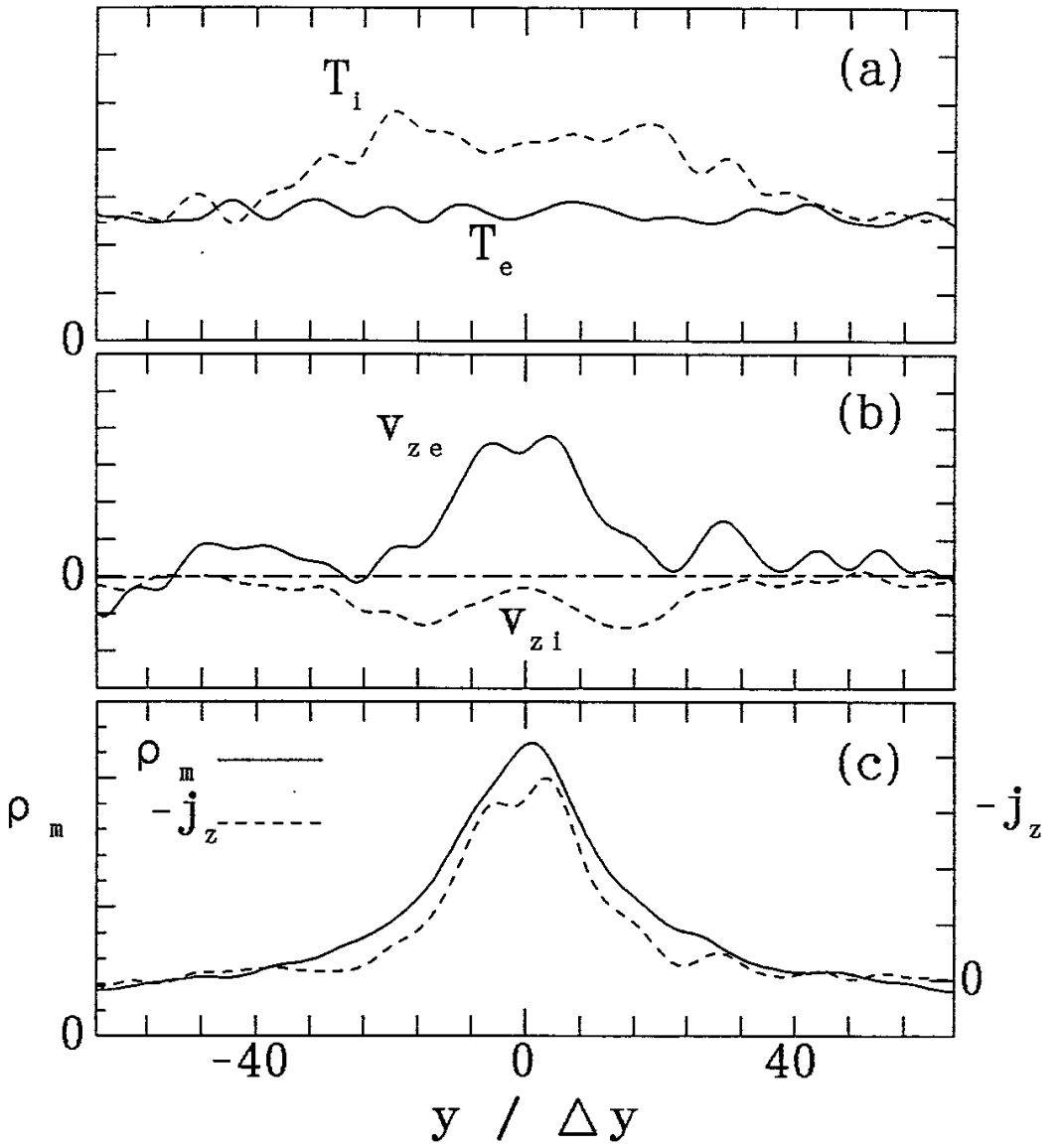

Figure 5

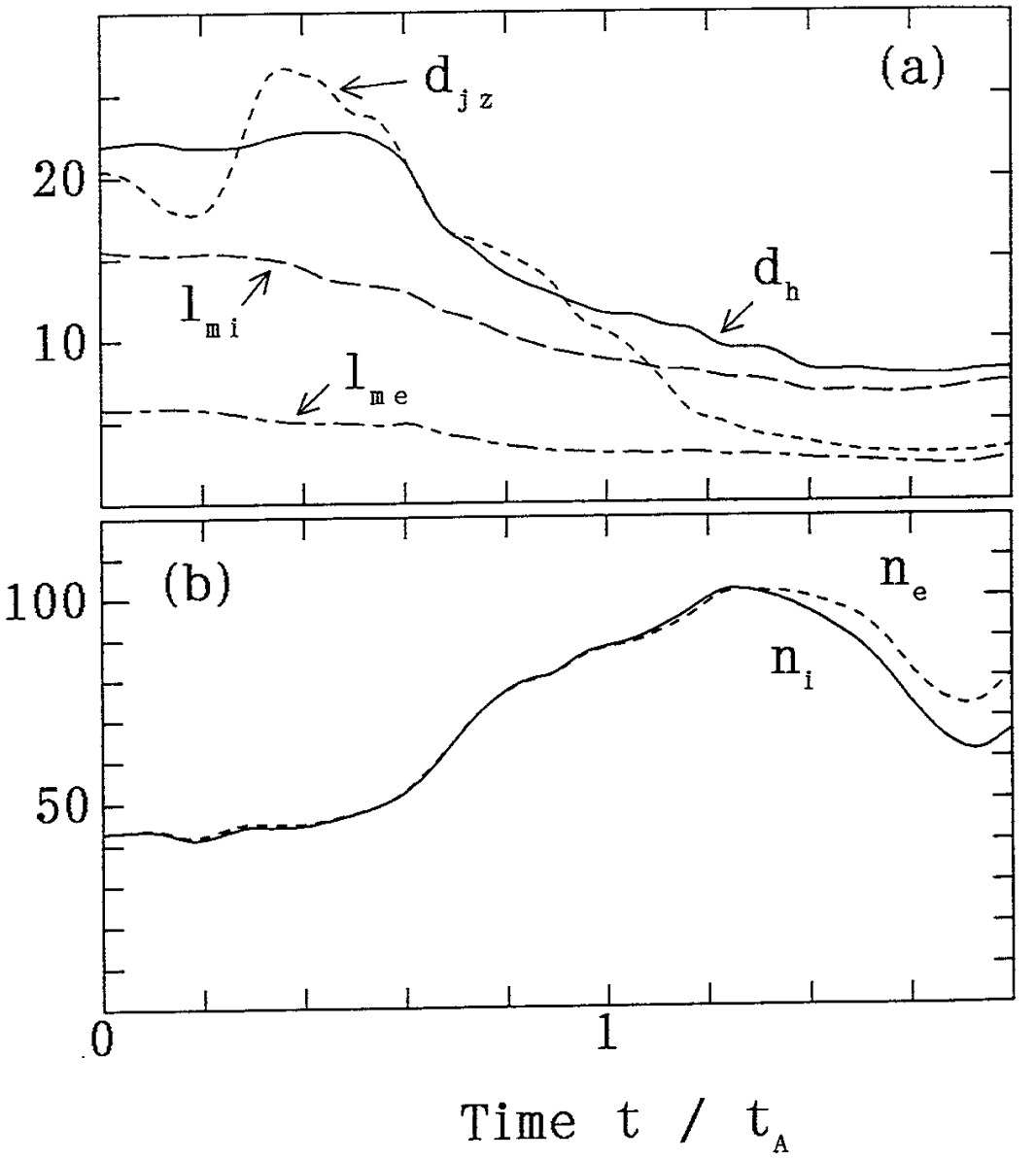

Figure 6

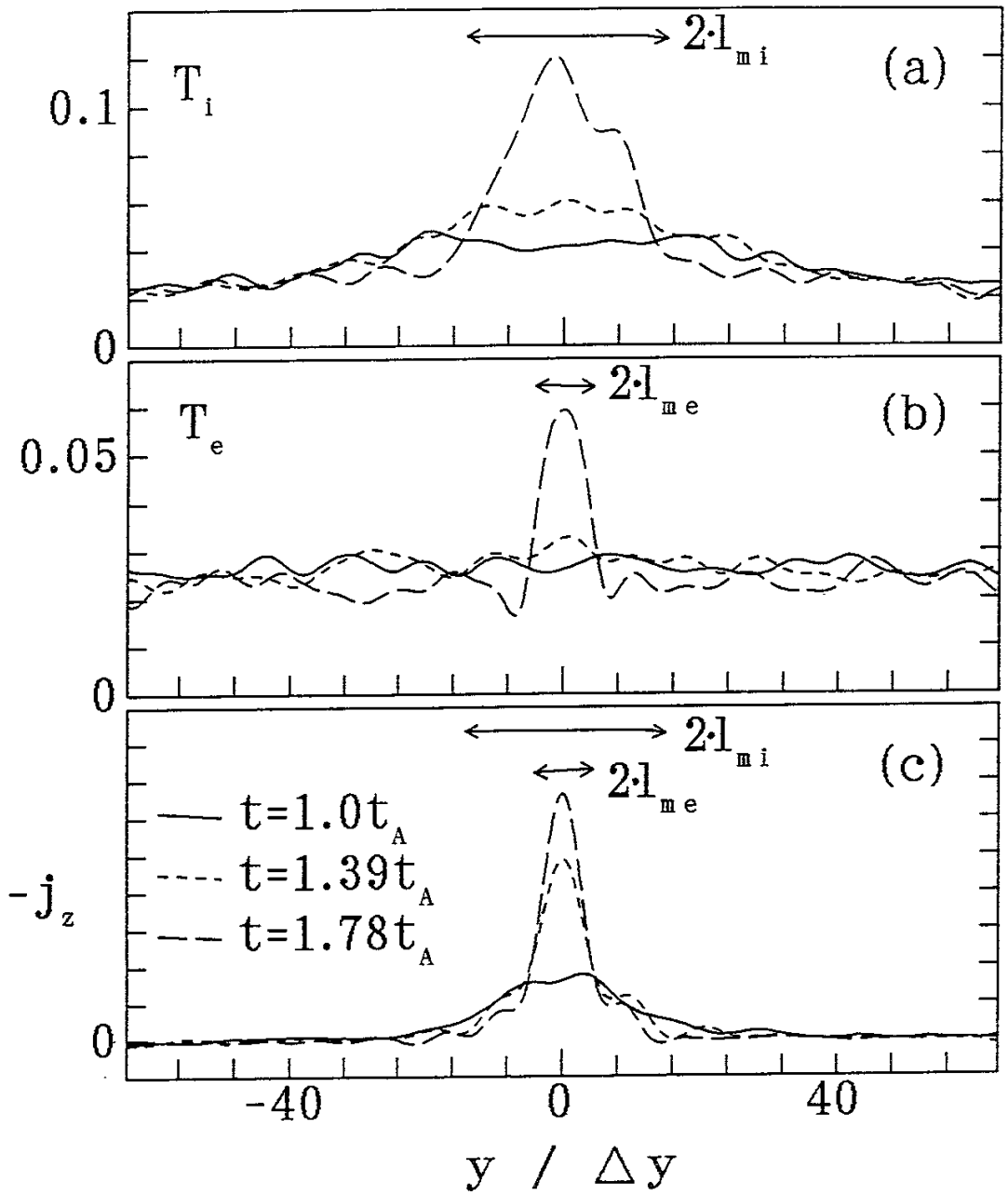
0.1
0
T_i
$2 \cdot l_{mi}$
(a)
0.05
0
T_e
$2 \cdot l_{me}$
(b)
$2 \cdot l_{mi}$
$2 \cdot l_{me}$
(c)
$t=1.0t_A$
$t=1.39t_A$
$t=1.78t_A$
$-j_z$
0
-40
0
40
$y / \Delta y$

Figure 7

Mass Density

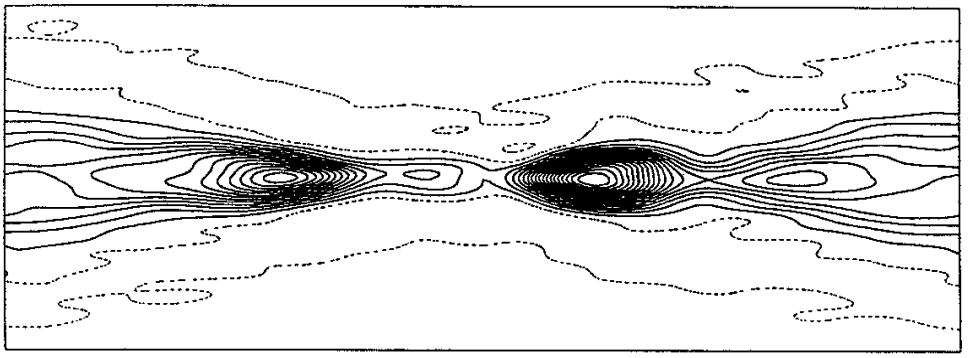

Current Density J_z

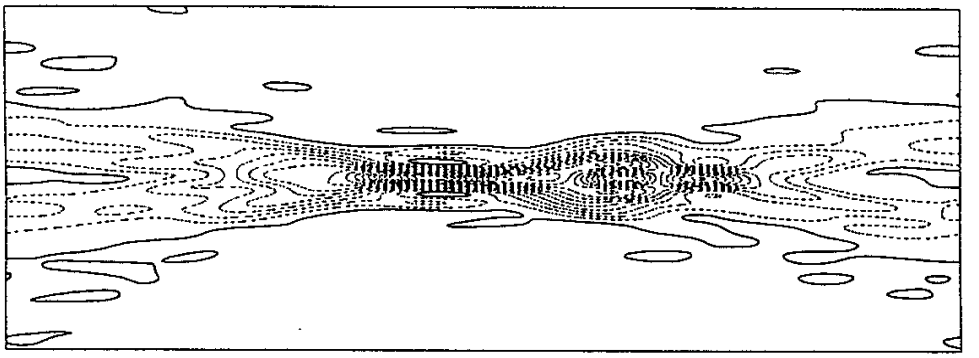

Electron Temperature

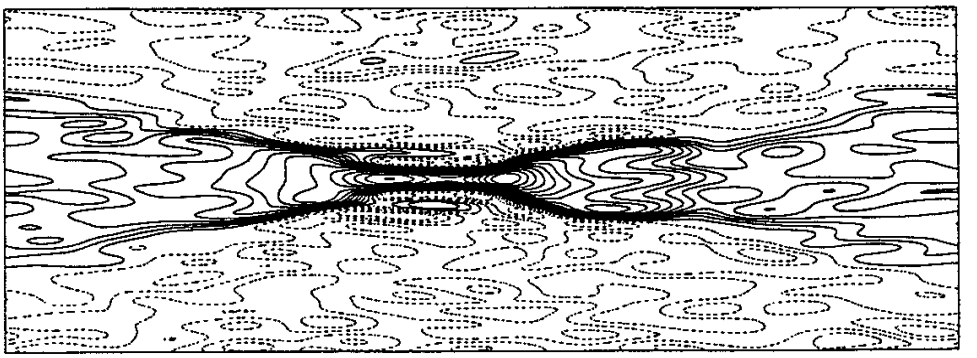

Ion Temperature

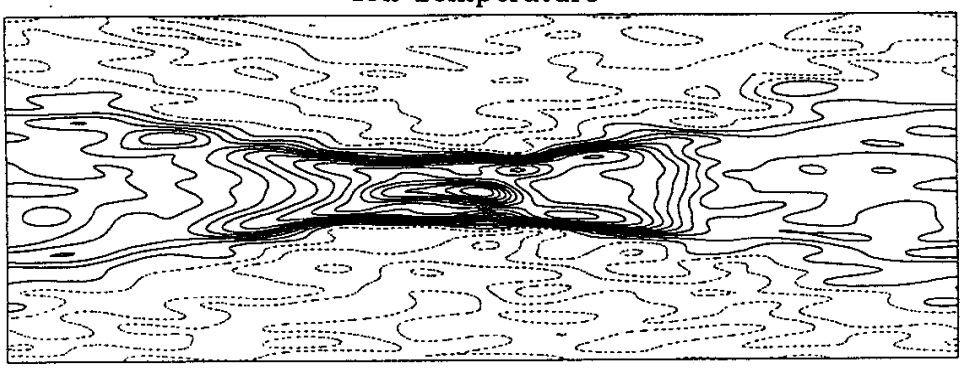

Figure 8

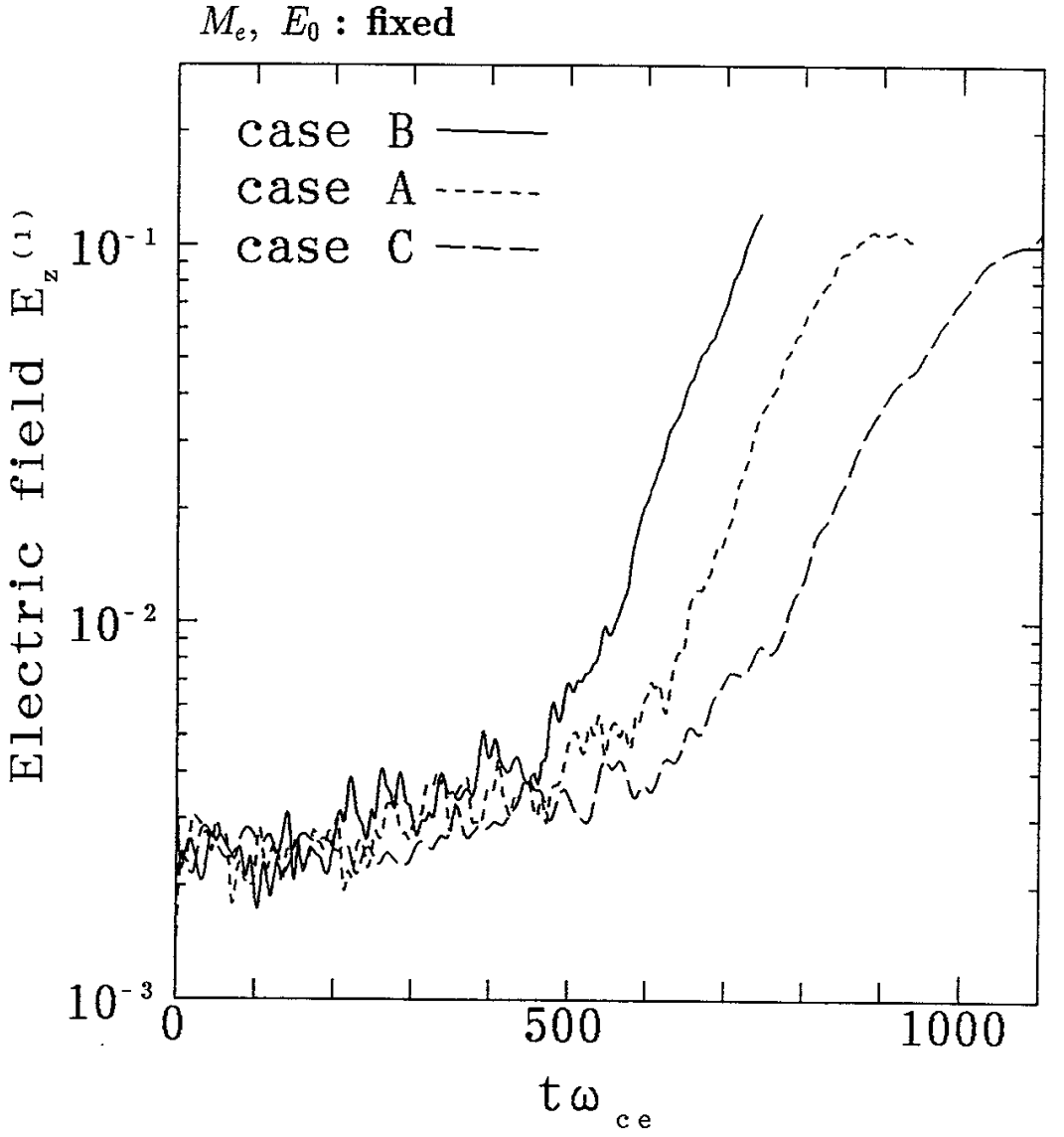
M_e, E_0 : fixed
case B
case A
case C
Electric field $E_z^{(1)}$
10^{-1}
10^{-2}
10^{-3}
0
500
1000
$t\omega_{ce}$

Figure 9

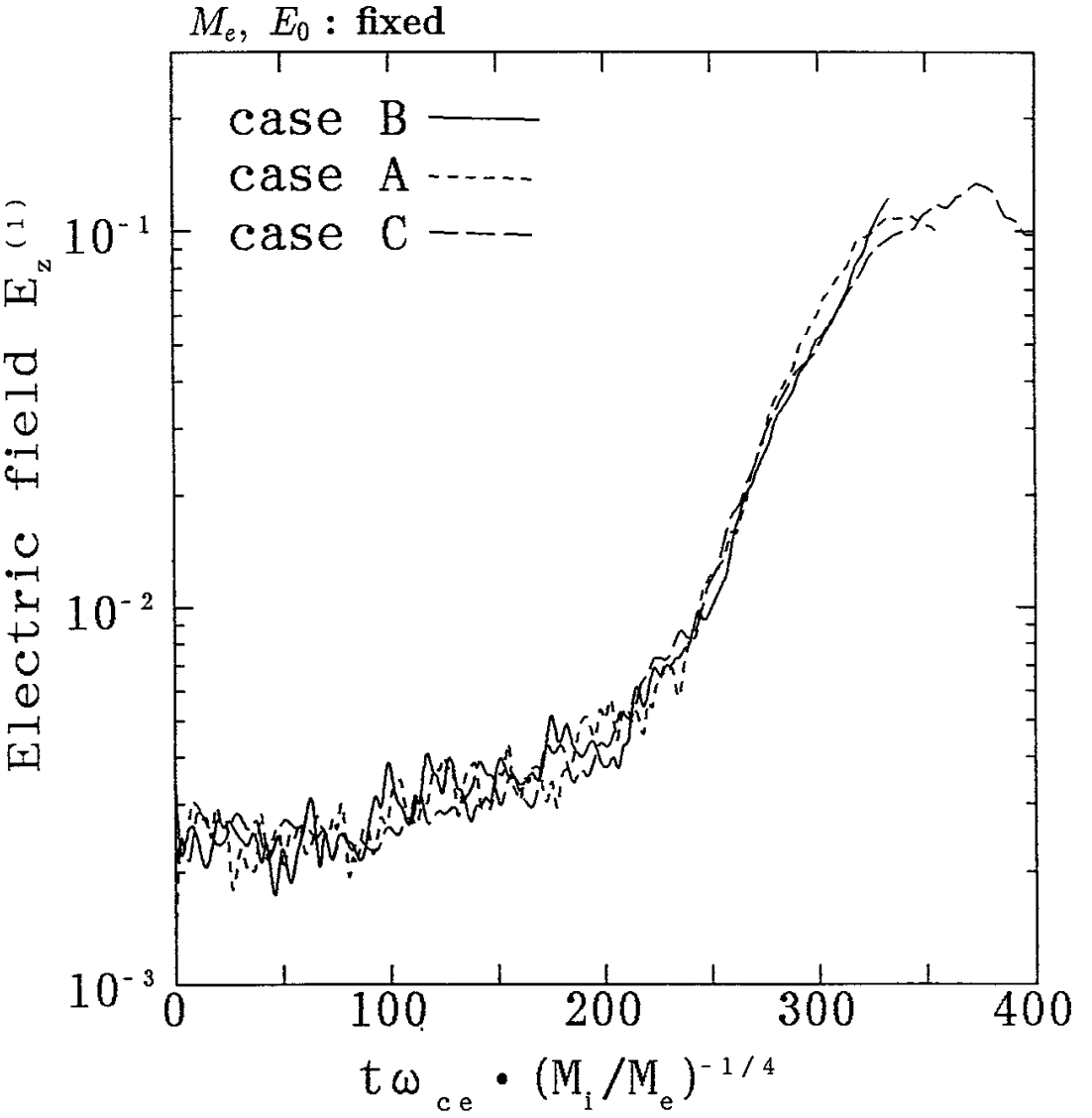
M_e, E_0 : fixed
case B
case A
case C
Electric field $E_z^{(1)}$
10^{-1}
10^{-2}
10^{-3}
0
100
200
300
400
$t\omega_{ce} \cdot (M_i/M_e)^{-1/4}$

Figure 10

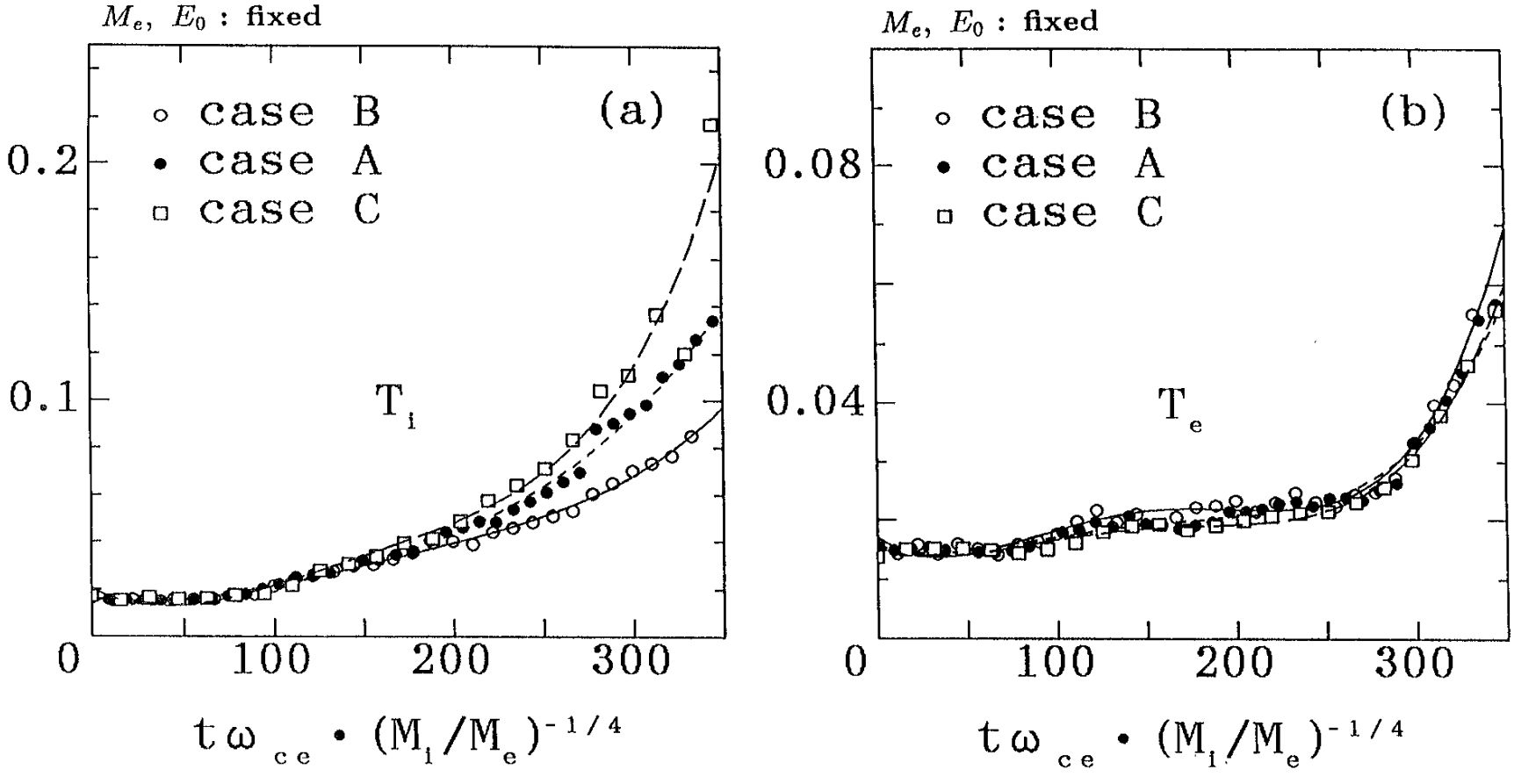
M_e, E_0 : fixed
case B
case A
case C
(a)
0.2
0.1
0
T_i
100
200
300
$t\omega_{ce} \cdot (M_i/M_e)^{-1/4}$
M_e, E_0 : fixed
case B
case A
case C
(b)
0.08
0.04
0
T_e
100
200
300
$t\omega_{ce} \cdot (M_i/M_e)^{-1/4}$

Figure 11

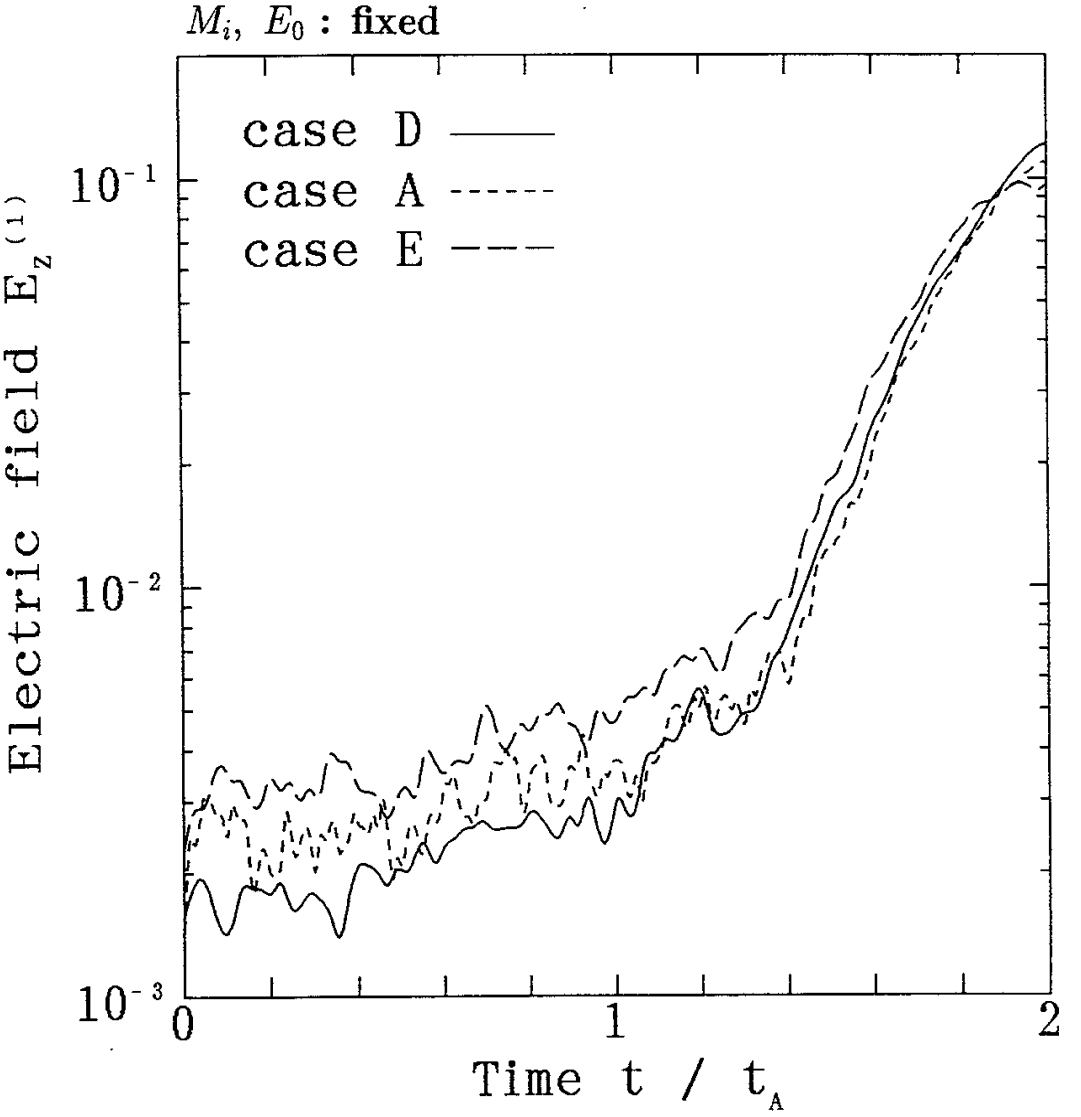
M_i, E_0 : fixed
case D
case A
case E
Electric field $E_z^{(1)}$
10^{-1}
10^{-2}
10^{-3}
0
1
2
Time t / t_A

Figure 12

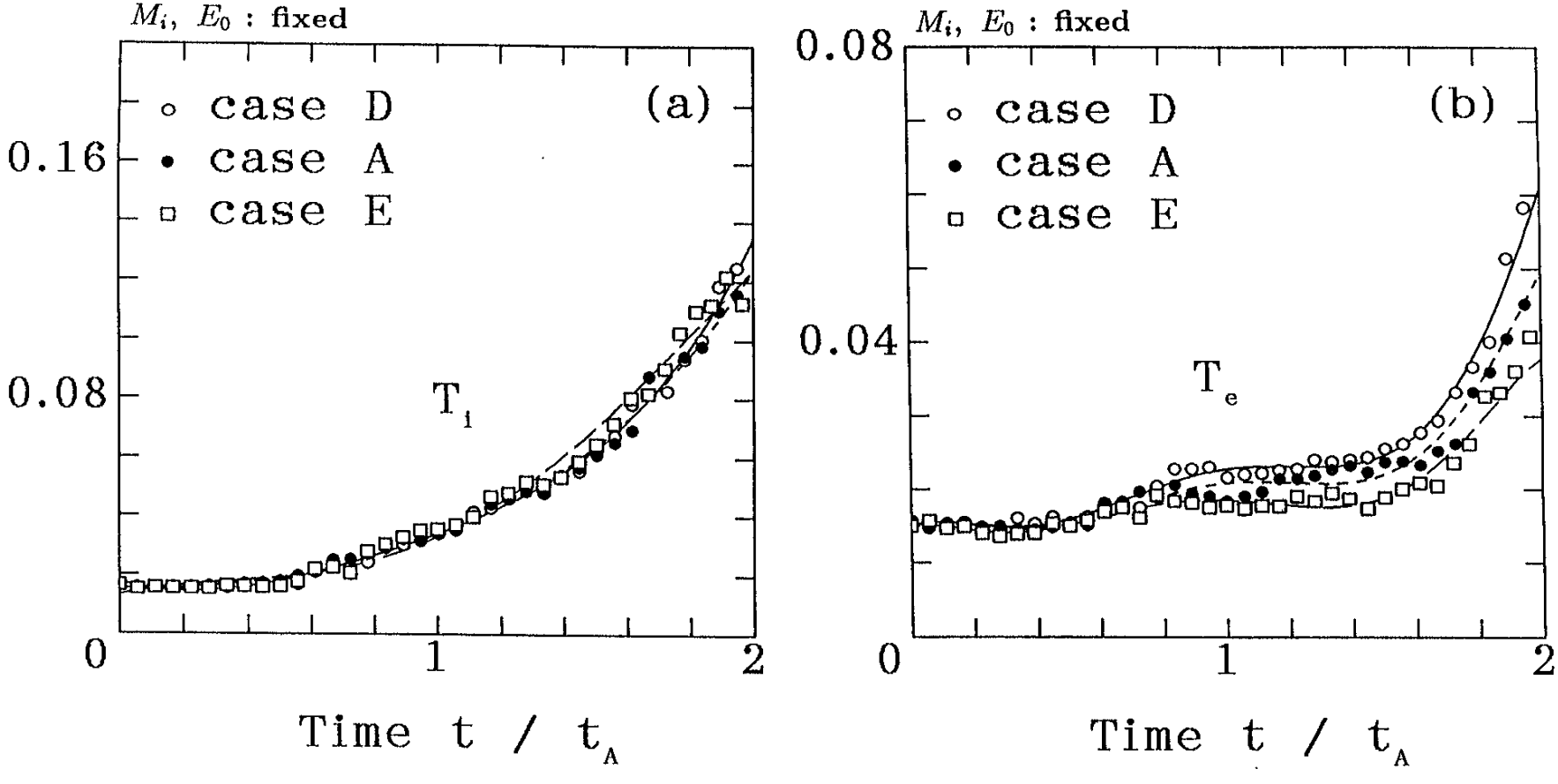
M_i, E_0 : fixed
case D
case A
case E
(a)
T_i
0.16
0.08
0
1
2
Time t / t_A
M_i, E_0 : fixed
case D
case A
case E
(b)
T_e
0.08
0.04
0
1
2
Time t / t_A

Figure 13

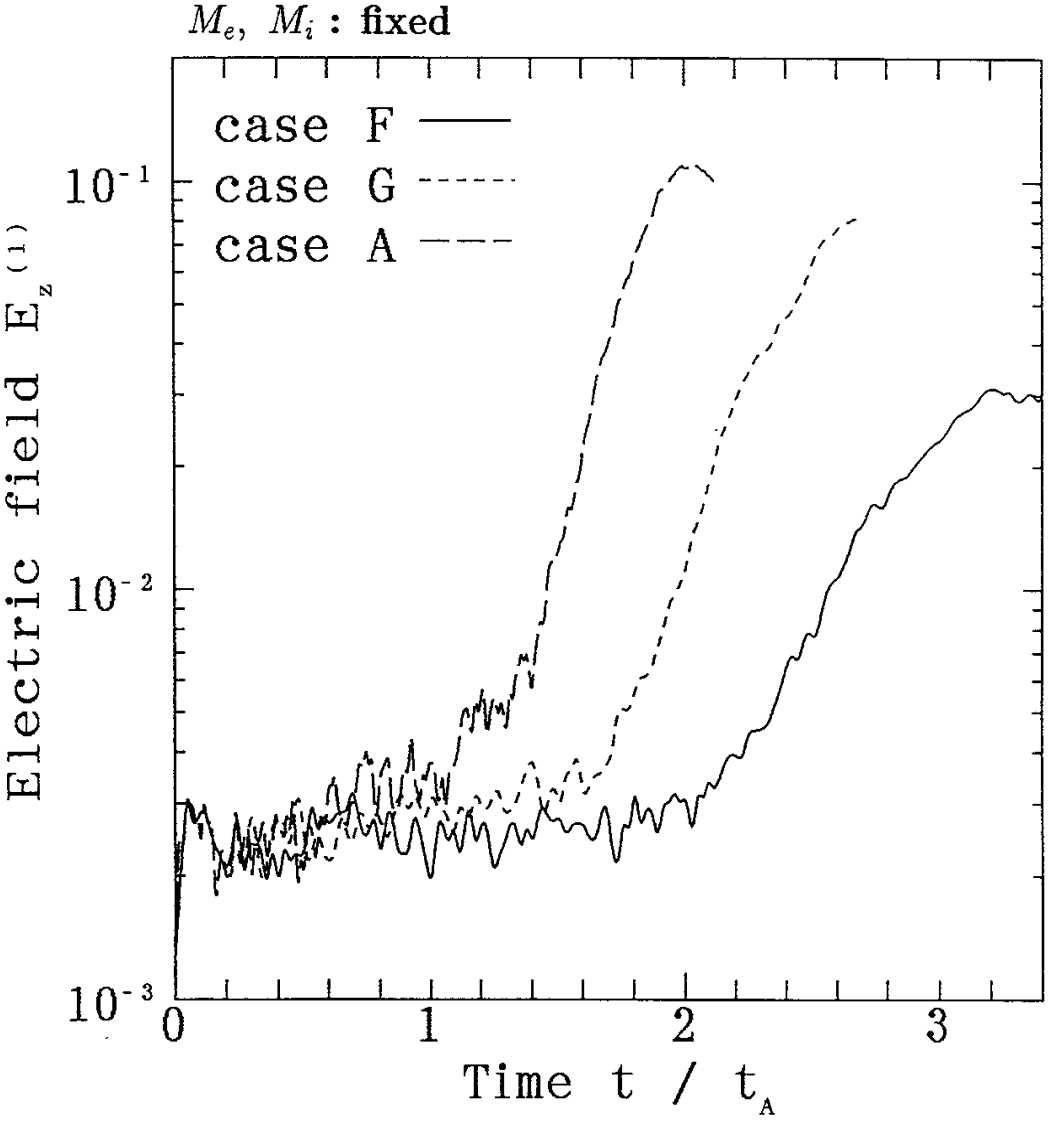
M_e, M_i : fixed
case F
case G
case A
10^{-1}
10^{-2}
10^{-3}
Electric field $E_z^{(1)}$
0
1
2
3
Time t / t_A

Figure 14

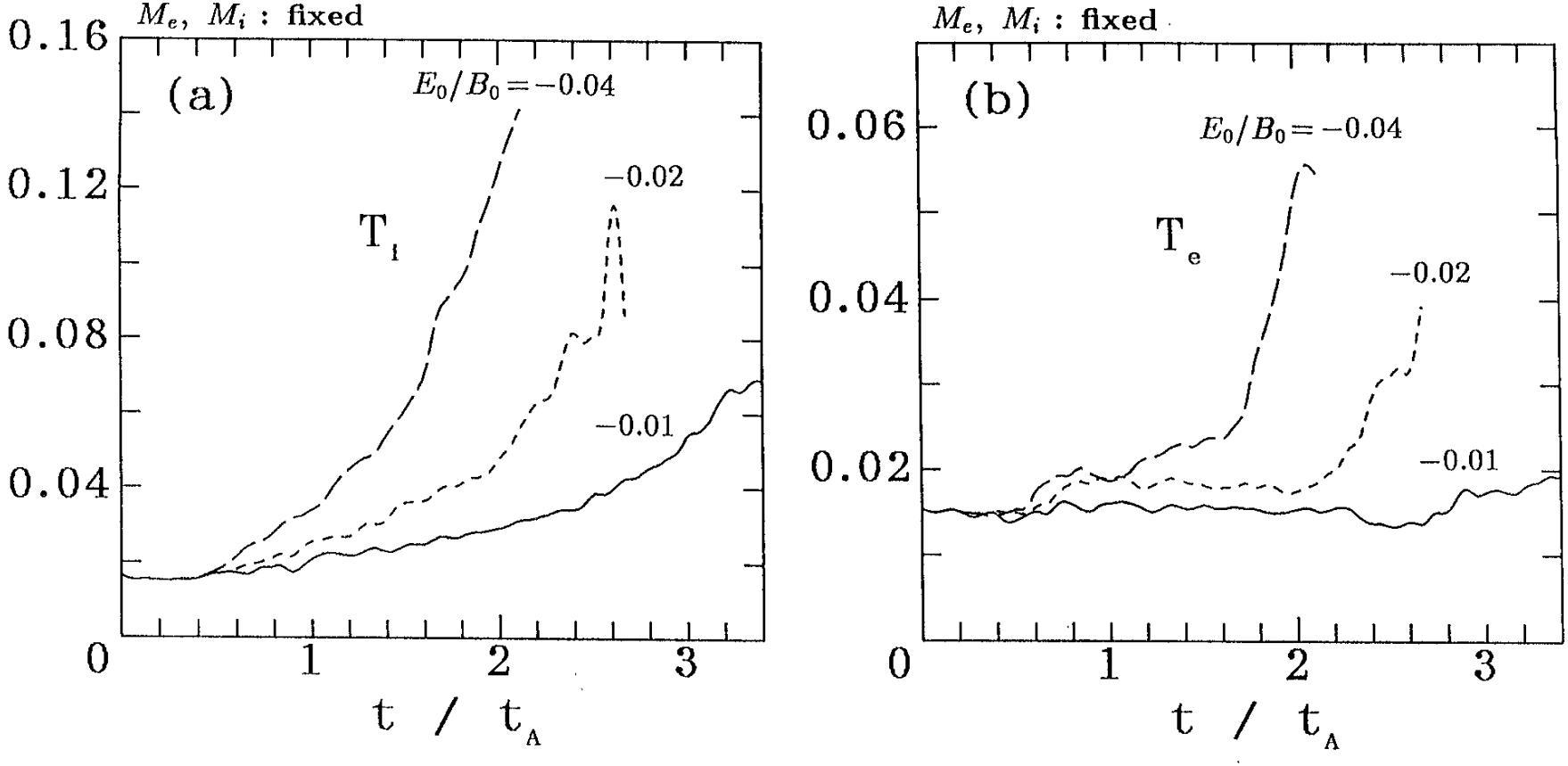
M_e, M_i : fixed
(a)
$E_0/B_0 = -0.04$
−0.02
−0.01
T_i
0.16
0.12
0.08
0.04
0
1
2
3
t / t_A
M_e, M_i : fixed
(b)
$E_0/B_0 = -0.04$
−0.02
−0.01
T_e
0.06
0.04
0.02
0
1
2
3
t / t_A

Figure 15

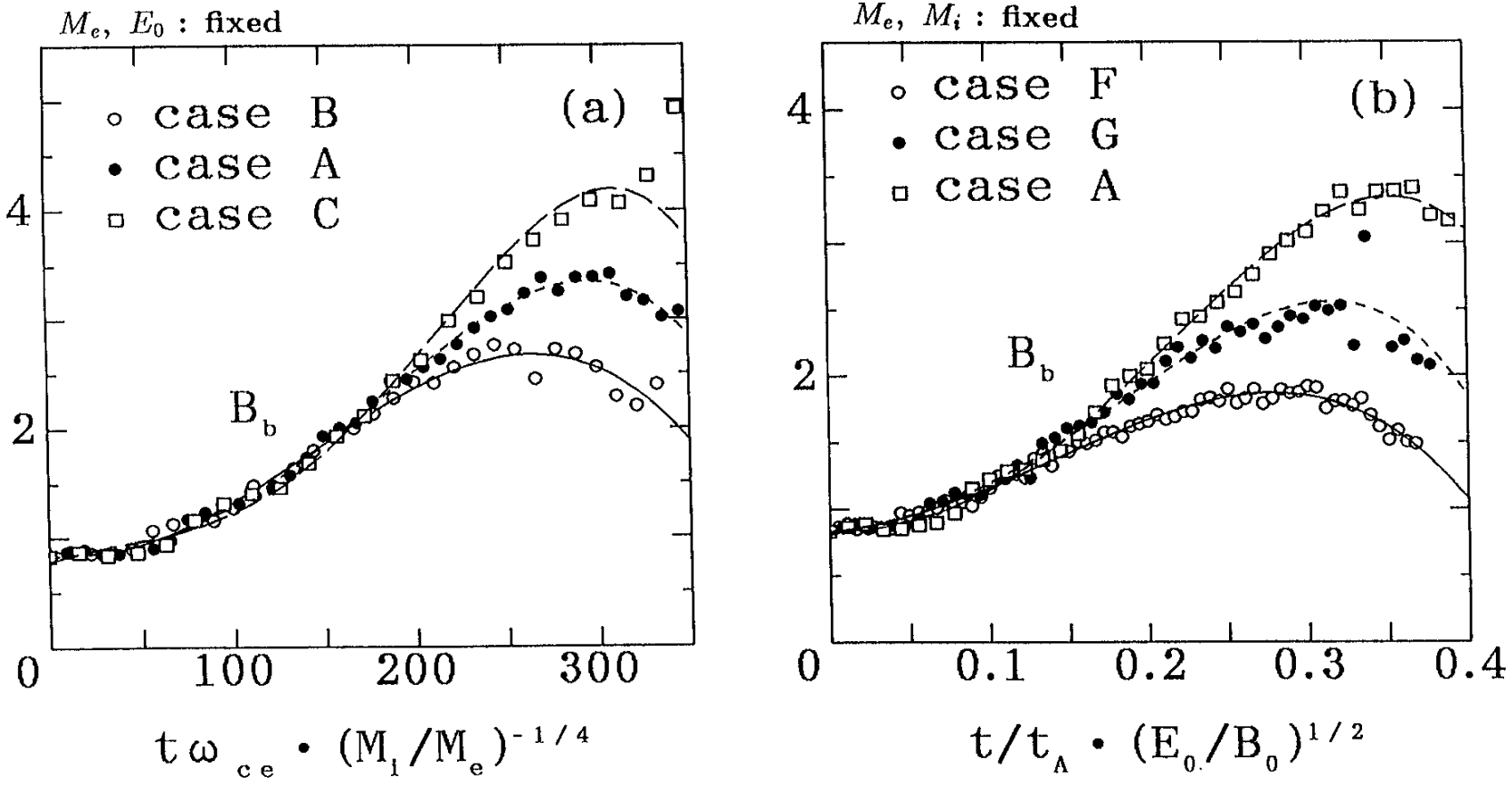
M_e, E_0 : fixed
case B
case A
case C
(a)
B_b
0
2
4
100
200
300
$t\omega_{ce} \cdot (M_i/M_e)^{-1/4}$
M_e, M_i : fixed
case F
case G
case A
(b)
B_b
0
2
4
0.1
0.2
0.3
0.4
$t/t_A \cdot (E_0/B_0)^{1/2}$

Recent Issues of NIFS Series

NIFS-239 N. Ohyabu, T. Watanabe, Hantao Ji, H. Akao, T. Ono, T. Kawamura, K. Yamazaki, K. Akaishi, N. Inoue, A. Komori, Y. Kubota, N. Noda, A. Sagara, H. Suzuki, O. Motojima, M. Fujiwara, A. Iiyoshi, *LHD Helical Divertor;* July 1993

NIFS-240 Y. Miura, F. Okano, N. Suzuki, M. Mori, K. Hoshino, H. Maeda, T. Takizuka, JFT-2M Group, K. Itoh and S.-I. Itoh, *Ion Heat Pulse after Sawtooth Crash in the JFT-2M Tokamak;* Aug. 1993

NIFS-241 K. Ida, Y.Miura, T. Matsuda, K. Itoh and JFT-2M Group, *Observation of non Diffusive Term of Toroidal Momentum Transport in the JFT-2M Tokamak;* Aug. 1993

NIFS-242 O.J.W.F. Kardaun, S.-I. Itoh, K. Itoh and J.W.P.F. Kardaun, *Discriminant Analysis to Predict the Occurrence of ELMS in H-Mode Discharges;* Aug. 1993

NIFS-243 K. Itoh, S.-I. Itoh, A. Fukuyama, *Modelling of Transport Phenomena;* Sep. 1993

NIFS-244 J. Todoroki, *Averaged Resistive MHD Equations;* Sep. 1993

NIFS-245 M. Tanaka, *The Origin of Collisionless Dissipation in Magnetic Reconnection;* Sep. 1993

NIFS-246 M. Yagi, K. Itoh, S.-I. Itoh, A. Fukuyama and M. Azumi, *Current Diffusive Ballooning Mode in Seecond Stability Region of Tokamaks;* Sep. 1993

NIFS-247 T. Yamagishi, *Trapped Electron Instabilities due to Electron Temperature Gradient and Anomalous Transport;* Oct. 1993

NIFS-248 Y. Kondoh, *Attractors of Dissipative Structure in Three Disspative Fluids;* Oct. 1993

NIFS-249 S. Murakami, M. Okamoto, N. Nakajima, M. Ohnishi, H. Okada, *Monte Carlo Simulation Study of the ICRF Minority Heating in the Large Helical Device;* Oct. 1993

NIFS-250 A. Iiyoshi, H. Momota, O. Motojima, M. Okamoto, S. Sudo, Y. Tomita, S. Yamaguchi, M. Ohnishi, M. Onozuka, C. Uenosono, *Innovative Energy Production in Fusion Reactors;* Oct. 1993

NIFS-251 H. Momota, O. Motojima, M. Okamoto, S. Sudo, Y. Tomita, S. Yamaguchi, A. Iiyoshi, M. Onozuka, M. Ohnishi, C. Uenosono, *Characteristics of D-^{3}He Fueled FRC Reactor: ARTEMIS-L,* Nov. 1993

NIFS-252 Y. Tomita, L.Y. Shu, H. Momota, *Direct Energy Conversion System for D-^{3}He Fusion,* Nov. 1993

NIFS-253 S. Sudo, Y. Tomita, S. Yamaguchi, A. Iiyoshi, H. Momota, O. Motojima, M. Okamoto, M. Ohnishi, M. Onozuka, C. Uenosono, *Hydrogen Production in Fusion Reactors,* Nov. 1993

NIFS-254 S. Yamaguchi, A. Iiyoshi, O. Motojima, M. Okamoto, S. Sudo, M. Ohnishi, M. Onozuka, C. Uenosono, *Direct Energy Conversion of Radiation Energy in Fusion Reactor,* Nov. 1993

NIFS-255 S. Sudo, M. Kanno, H. Kaneko, S. Saka, T. Shirai, T. Baba, *Proposed High Speed Pellet Injection System "HIPEL" for Large Helical Device* Nov. 1993

NIFS-256 S. Yamada, H. Chikaraishi, S. Tanahashi, T. Mito, K. Takahata, N. Yanagi, M. Sakamoto, A. Nishimura, O. Motojima, J. Yamamoto, Y. Yonenaga, R. Watanabe, *Improvement of a High Current DC Power Supply System for Testing the Large Scaled Superconducting Cables and Magnets*; Nov. 1993

NIFS-257 S. Sasaki, Y. Uesugi, S. Takamura, H. Sanuki, K. Kadota, *Temporal Behavior of the Electron Density Profile During Limiter Biasing in the HYBTOK-II Tokamak*; Nov. 1993

NIFS-258 K. Yamazaki, H. Kaneko, S. Yamaguchi, K.Y. Watanabe, Y.Taniguchi, O.Motojima, LHD Group, *Design of Central Control System for Large Helical Device (LHD)*; Nov. 1993

NIFS-259 S. Yamada, T. Mito, A. Nishimura, K. Takahata, S. Satoh, J. Yamamoto, H. Yamamura, K. Masuda, S. Kashihara, K. Fukusada, E. Tada, *Reduction of Hydrocarbon Impurities in 200L/H Helium Liquefier-Refrigerator System*; Nov. 1993

NIFS-260 B.V.Kuteev, *Pellet Ablation in Large Helical Device*; Nov. 1993

NIFS-261 K. Yamazaki, *Proposal of "MODULAR HELIOTRON': Advanced Modular Helical System Compatible with Closed Helical Divertor*; Nov. 1993

NIFS-262 V.D.Pustovitov,
Some Theoretical Problems of Magnetic Diagnostics in Tokamaks and Stellarators; Dec. 1993

NIFS-263 A. Fujisawa, H. Iguchi, Y. Hamada
A Study of Non-Ideal Focus Properties of 30° Parallel Plate Energy Analyzers; Dec. 1993

NIFS-264 K. Masai,
Nonequilibria in Thermal Emission from Supernova Remnants; Dec. 1993

NIFS-265 K. Masai, K. Nomoto,
X-Ray Enhancement of SN 1987A Due to Interaction with its Ring-like Nebula; Dec. 1993

NIFS-266 J. Uramoto
A Research of Possibility for Negative Muon Production by a Low Energy Electron Beam Accompanying Ion Beam; Dec. 1993

NIFS-267 H. Iguchi, K. Ida, H. Yamada, K. Itoh, S.-I. Itoh, K. Matsuoka, S. Okamura, H. Sanuki, I. Yamada, H. Takenaga, K. Uchino, K. Muraoka,
The Effect of Magnetic Field Configuration on Particle Pinch Velocity in Compact Helical System (CHS); Jan. 1994

NIFS-268 T. Shikama, C. Namba, M. Kosuda, Y. Maeda,
Development of High Time-Resolution Laser Flash Equipment for Thermal Diffusivity Measurements Usting Miniature-Size Specimens; Jan. 1994

NIFS-269 T. Hayashi, T. Sato, P. Merkel, J. Nührenberg, U. Schwenn,
Formation and 'Self-Healing' of Magnetic Islands in Finite-β Helias Equilibria; Jan. 1994

NIFS-270 S. Murakami, M. Okamoto, N. Nakajima, T. Mutoh,
Efficiencies of the ICRF Minority Heating in the CHS and LHD Plasmas; Jan. 1994

NIFS-271 Y. Nejoh, H. Sanuki,
Large Amplitude Langmuir and Ion-Acoustic Waves in a Relativistic Two-Fluid Plasma; Feb. 1994

NIFS-272 A. Fujisawa, H. Iguchi, A. Taniike, M. Sasao, Y. Hamada,
A 6MeV Heavy Ion Beam Probe for the Large Helical Device; Feb. 1994

NIFS-273 Y. Hamada, A. Nishizawa, Y. Kawasumi, K. Narihara, K. Sato, T. Seki, K. Toi, H. Iguchi, A. Fujisawa, K. Adachi, A. Ejiri, S. Hidekuma,

S. Hirokura, K. Ida, J. Koong, K. Kawahata, M. Kojima, R. Kumazawa, H. Kuramoto, R. Liang, H. Sakakita, M. Sasao, K. N. Sato, T. Tsuzuki, J. Xu, I. Yamada, T. Watari, I. Negi,
Measurement of Profiles of the Space Potential in JIPP T-IIU Tokamak Plasmas by Slow Poloidal and Fast Toroidal Sweeps of a Heavy Ion Beam; Feb. 1994

NIFS-274 M. Tanaka,
A Mechanism of Collisionless Magnetic Reconnection; Mar. 1994

NIFS-275 A. Fukuyama, K. Itoh, S.-I. Itoh, M. Yagi and M. Azumi,
Isotope Effect on Confinement in DT Plasmas; Mar. 1994

NIFS-276 R.V. Reddy, K. Watanabe, T. Sato and T.H. Watanabe,
Impulsive Alfven Coupling between the Magnetosphere and Ionosphere; Apr.1994

NIFS-277 J. Uramoto,
A Possibility of π^- Meson Production by a Low Energy Electron Bunch and Positive Ion Bunch; Apr. 1994

NIFS-278 K. Itoh, S.-I. Itoh, A. Fukuyama, M. Yagi and M. Azumi,
Self-sustained Turbulence and L-mode Confinement in Toroidal Plasmas II; Apr. 1994

NIFS-279 K. Yamazaki and K.Y.Watanabe,
New Modular Heliotron System Compatible with Closed Helical Divertor and Good Plasma Confinement; Apr. 1994

NIFS-280 S. Okamura, K. Matsuoka, K. Nishimura, K. Tsumori, R. Akiyama, S. Sakakibara, H. Yamada, S. Morita, T. Morisaki,. N. Nakajima, K. Tanaka, J. Xu, K. Ida, H. Iguchi, A. Lazaros, T. Ozaki, H. Arimoto, A. Ejiri, M. Fujiwara, H. Idei. O. Kaneko, K. Kawahata, T. Kawamoto, A. Komori, S. Kubo, O. Motojima, V.D. Pustovitov, C. Takahashi, K. Toi and I. Yamada,
High-Beta Discharges with Neutral Beam Injection in CHS, Apr; 1994

NIFS-281 K. Kamada, H. Kinoshita and H. Takahashi,
Anomalous Heat Evolution of Deuteron Implanted Al on Electron Bombardment ; May 1994

NIFS-282 H. Takamaru, T. Sato, K. Watanabe and R. Horiuchi,
Super Ion Acoustic Double Layer; May 1994

NIFS-283 O.Mitarai and S. Sudo
Ignition Characteristics in D-T Helical Reactors; June 1994